Microtubule stiffening by ZYG-8 contributes to spindle orientation during *C. elegans* zygote division

Authors:
Louis Cueff[1], Ewen Huet[1], Loïc Schmitt[1], Sylvain Pastezeur[1], Méline Coquil[1], Titouan Savary[1], Jacques Pécréaux[1,*], Hélène Bouvrais[1,*]

Affiliations:
[1] IGDR CNRS, Univ Rennes, IGDR (Institut de Génétique et Développement de Rennes) – UMR 6290, F-35000 Rennes, France
* Corresponding authors :
Jacques Pécréaux (ORCID : 0000-0001-9998-4844) and Hélène Bouvrais (ORCID : 0000-0003-1128-1322)
IGDR-UMR6290, CNRS-Université de Rennes
Faculté de Médecine
2 Av. du Professeur Léon Bernard,
CS 34317 - 35043 Rennes Cedex
France
Tel: +33 2 23 23 45 03 (JP), +33 2 23 23 40 08 (HB)
Email: jacques.pecreaux@univ-rennes.fr, helene.bouvrais@univ-rennes.fr

ABSTRACT
In *Caenorhabditis elegans*, mutations in *zyg-8*^{DCLK1}, the sole Doublecortin-family member, led to incorrect mitotic spindle positioning, as seen by immunofluorescence. Doublecortin proteins bind to microtubules and are thought to stabilise or rigidify microtubules. Upon targeting *zyg-8*, we observed altered spindle-pole oscillations and perturbations in microtubule cortical-contact behaviour. They could not be explained by changes in microtubule dynamics alone. Instead, the phenotypes were consistent with ZYG-8 contributing to microtubule rigidity. Its depletion or mutation led to more frequent microtubule bending, and higher curvature and tortuosity. Microtubule softening in *zyg-8* mutants likely reduced the efficiency of centring forces, causing exaggerated spindle oscillations and subsequent mispositioning during late anaphase. We propose that sufficient microtubule rigidity is essential for generating effective cortical pushing forces, which act as centring mechanisms to ensure accurate spindle orientation during mitosis. These findings may have implications for cancer therapy, since the expression of DCLK1 and Tau, both known regulators of microtubule rigidity, is often deregulated in various human cancers.

INTRODUCTION

Microtubules are semi-rigid polymers that form a crucial component of the cell cytoskeleton alongside actin and intermediate filaments. In coordination with molecular motors and microtubule-associated proteins (MAPs), microtubules perform essential functions, including cell shaping[1, 2], intracellular trafficking[3], and cell migration[4]. Microtubules also play major roles in cell division; for example, spindle microtubules assemble into the mitotic spindle and segregate chromosomes, while astral microtubules help position the spindle[5-11]. Along a structural line, each microtubule comprises protofilaments that are linear chains of tubulin dimers added or removed dynamically. Microtubule dynamic instability, characterised by stochastic transitions between growing and shrinking phases, is regulated *in vivo* by numerous MAPs[12-14]. The mechanical properties of microtubules, particularly their flexural rigidity—i.e., their resistance to bending—have received comparatively less attention. Notably, microtubules exhibit the highest flexural rigidity among cytoskeletal filaments[15]. While *in vitro* reconstituted microtubules are bent at the scale of a few millimetres[15-18], *in vivo* observations revealed that microtubules appear bent at the micrometre scale[19-21]. On the one hand, high microtubule rigidity is necessary for efficient intracellular trafficking[22], for generating pushing forces against the cell periphery that contribute to spindle or nucleus positioning[23-28], or for exerting pushing forces on chromosome arms to produce the polar ejection force[29, 30]. On the other hand, microtubules must also be flexible enough to bend, for example when growing through the crowded cytoplasm[31]. This highlights the need to regulate microtubule flexural rigidity *in vivo* to support its various biological functions[21].

Research, particularly in neuronal systems, has identified two major protein families involved in regulating microtubule rigidity. These are the Doublecortin family, which includes DCX and DCLK1, and the MAP2/MAP4/Tau superfamily[16, 18, 32, 33]. For instance, the simultaneous knockdown of DCX and DCLK1 in rat neurons led to more curved microtubules at the growing axon tip[34]. Doublecortin-family proteins associate with microtubules through their doublecortin domains. Notably, these proteins bind between the microtubule protofilaments at the vertices of four tubulin dimers, contributing to the lateral coupling of adjacent protofilaments[35, 36]. This binding likely restricts protofilament sliding, thereby increasing microtubule rigidity[37, 38]. Along a similar line, Tau-deficient axons have been shown to exhibit curled microtubules[39]. Tau family proteins bind longitudinally along the outer ridges of microtubule protofilaments. It would strengthen the longitudinal contacts between tubulin heterodimers within a protofilament, straightening the protofilaments[32, 40, 41]. Importantly, both protein families could also contribute to the regulation of microtubule dynamics, making it challenging to disentangle their roles in mechanical versus dynamic regulation. Some *in vivo* studies indicate that these proteins stabilise microtubules and/or promotes their growth[39, 42]. They may reduce their dynamics by decreasing catastrophe frequency, depolymerisation and nucleation rates[42-44]. While the impacts of controlling microtubule rigidity have primarily been studied in neurons, microtubule-rigidity contribution during cell division also warrants investigations.

Previous studies on cell division involving the targeting of proteins from the Doublecortin and Tau families revealed several defects. These included mitotic spindle mispositioning, abnormalities in the formation and integrity of meiotic or mitotic spindles, and impaired mitotic progression[45-51]. During neurogenesis, altered expression of Doublecortin-family proteins led to incorrect cell fate determination for neural progenitors[45, 46]. Additionally, the

deregulation of Tau (whether through mutation or overexpression) resulted in mitotic defects, such as issues with spindle formation, aneuploidy and chromosome misalignment[52, 53]. Thus, targeting Doublecortin and Tau family proteins can lead to a wide range of meiotic and mitotic disturbances, although the underlying mechanisms remain unclear. Proposed explanations include perturbations in microtubule stability, and in molecular motor activity or recruitment[45-50, 54]. Whether the underlying mechanism could involve microtubule rigidity is yet to be investigated.

In the *Caenorhabditis elegans* zygote, the pronuclei-centrosome complex (NCC) and the mitotic spindle exhibit stereotyped movements during cell division[55]. It makes this system a well-established model for studying asymmetric divisions. In these divisions, the correct positioning and orientation of the spindle are critical for cell fate determination and, more broadly, for the organism's development[9]. In further detail, the NCC forms at the zygote posterior pole, migrates anteriorly, and the centrosomes align with the anteroposterior axis during prophase. The mitotic spindle assembles near the cell centre after the nuclear envelop breakdown (NEBD), remains centred during metaphase, and is then positioned posteriorly, mainly during anaphase[56]. During this posterior displacement, the spindle undergoes transverse oscillations driven by strong cortical pulling forces[57]. While not essential for asymmetric division, these oscillations have been instrumental in studying spindle positioning forces[58-63]. Astral microtubules, which emanate from the centrosomes, play a central role in spindle movements. These microtubules can transmit or generate three types of forces[5, 7, 64]: first, cortical pulling forces mediated by dynein motors anchored at the cell cortex interacting with shrinking microtubules[58, 65, 66]; second, cytoplasmic pulling forces that are reaction forces generated by organelle movement along microtubules, driven by dynein motors[67]; and third, cortical pushing forces generated by microtubules that grow against the cell cortex[25, 27, 68]. Various models have addressed the roles of these forces. Kimura *et al.* proposed that cytoplasmic pulling forces contribute to NCC centration[67], while others have suggested that these forces do not aid in maintaining spindle position at the cell centre during metaphase[25] or in driving anaphase spindle oscillations[59]. Cortical pulling forces, which are stronger at the posterior, are well-established drivers of posterior spindle displacement and anaphase oscillations[58-60, 66, 69, 70]. However, a restoring force must exist during spindle-pole oscillations, notably to stabilise the spindle position against these strong cortical pulling forces and permit oscillations. This centring mechanism could arise from the embryo's geometry[59, 66] or microtubule dynamics[58]. Alternative mechanisms include cytoplasmic pulling forces or cortical pushing forces. The latter may result from astral microtubules pushing against the cortex or from microtubule buckling[27, 57, 58]. We and others suggested that microtubule buckling—bending under compressive load—contributes to centring the spindle, in particular for spindle maintenance at the cell centre during metaphase[25, 27, 68, 71]. It makes the flexural rigidity of microtubules as a candidate key factor in spindle choreography. We envisioned that sufficiently high microtubule rigidity is necessary to enable stronger cortical pushing forces. These forces may be required to counterbalance elevated cortical pulling forces during anaphase.

In *C. elegans* zygote, mutations in *zyg-8^{dclk1}*, the sole Doublecortin family member, have been shown to cause improper spindle positioning during anaphase, as observed through immunofluorescence and DIC microscopy[48, 72] ZYG-8 contains a kinase domain at the C-terminus and two doublecortin (DC) domains at the N-terminus, the latter enabling its binding to microtubules. Studies of the human homolog DCLK1 revealed that its kinase domain auto-

phosphorylates the DC domains. Besides, hyperphosphorylation of these domains reduces DCLK1's binding affinity to microtubules[73]. In *C. elegans* zygote, mutations in either domain of *zyg-8* led to spindle orientation defects[48]. It has been proposed that ZYG-8 promotes microtubule assembly, which is required for correct spindle positioning[48, 72]. Interestingly, Srayko *et al.* found that ZYG-8 modestly contributes to microtubule growth, particularly when compared to the known polymerase ZYG-9[42]. Besides, ZYG-8 was shown to slightly limit astral microtubule nucleation, though the perturbations were less pronounced than those seen with *spd-2(RNAi)*[42]. Could these moderate effects on microtubule dynamics cause by *zyg-8* targeting be sufficient to explain the spindle mis-positioning seen in *zyg-8* mutants during anaphase? To address this question and better understand ZYG-8's role in spindle positioning, we used modern microscopy techniques that allow dynamic studies in live embryos, along with advanced image analysis. We explored the potential roles of ZYG-8 in regulating both microtubule dynamics and flexural rigidity. We applied three complementary genetic perturbations: RNAi-mediated depletion of ZYG-8, overexpression, and the thermosensitive *zyg-8(or484ts)* mutant that disrupts microtubule binding[72]. Upon targeting *zyg-8*, we analysed anaphase spindle oscillations and microtubule cortical contact behaviour. We found that the observed changes could not be explained solely by altered microtubules dynamics. This prompted us to investigate whether ZYG-8 also regulates microtubule rigidity during zygote division. To assess changes in microtubule rigidity, we measured the distributions of microtubule local curvatures. We also examined spindle positioning forces using a range of biophysical approaches. Our results demonstrate that ZYG-8 is needed to maintain the correct spindle orientation during mitosis, primarily by permitting high centring forces that depend on the microtubule flexural rigidity. Interestingly, RNAi depletion of PTL-1, the sole member of the Tau/MAPT family, produced a similar but milder effect on spindle choreography. Overall, our study highlights the need for sufficient microtubule rigidity for proper mitotic spindle positioning and orientation during *C. elegans* zygote division.

RESULTS

1- ZYG-8 affects spindle-pole oscillations beyond microtubule growth and nucleation.

In *C. elegans* zygotes, mutations in *zyg-8*^{dclk1} disrupted spindle positioning, particularly during anaphase, as shown by DIC microscopy recordings[48, 72]. These mutations were proposed to perturb astral microtubule stability, as microtubules stained with anti-tubulin antibodies appeared shorter. Immunofluorescence revealed that ZYG-8 localises at least to the spindle and its poles[48]. To investigate its association with astral microtubules, we generated three strains using CRISPR-Cas9 genome editing: one expressing fluorescently tagged ZYG-8 (mNeonGreen::ZYG-8) from the endogenous locus; a second with *zyg-8* tagged at the locus with three OLLAS epitope tags; and a third carrying an integrated transgene overexpressing *zyg-8* (*pPie-1*::mNG::3*OLLAS::ZYG-8) in addition to the endogenous copy (Table S1). During the first embryonic division, in both endogenously expressed and overexpressed *zyg-8* strains, ZYG-8 showed significant co-localisation with astral and spindle microtubules (Figure S1, Method M5). This localisation was consistent with its previously proposed role in promoting microtubule assembly[48].

Previous studies in *C. elegans* zygotes focussing on ZYG-8 have either examined its role in spindle positioning using *zyg-8* mutants or investigated its effects on microtubule dynamics through *zyg-8(RNAi)* treatment[42, 48, 72]. We sought to complement these studies by introducing

three distinct genetic perturbations targeting *zyg-8*. First, we used the thermosensitive mutant *zyg-8(or484ts)*, which carries a mutation in the first doublecortin domain[48, 74]. This mutant has been reported to prevent ZYG-8's ability to bind microtubules when maintained at the restrictive temperature of 25°C for more than 12 hours[72]. Second, we used the strain described above that overexpresses ZYG-8. Western blot analysis of worm lysates revealed increased OLLAS levels, indicated elevated ZYG-8 expression, as the OLLAS tag was inserted into the overexpression transgene (Figure S2A, Method M6). Besides, mNG::ZYG-8 fluorescence on both spindle and astral microtubules in zygotes increased approximately threefold (Figure S2C, D & G, Method M6). Third, we reduced ZYG-8 expression using RNAi. Western blot analysis of worm lysates from the strain carrying OLLAS-tagged *zyg-8* showed decreased OLLAS levels upon *zyg-8(RNAi)*, indicating reduced ZYG-8 expression (Figure S2B, Method M6). Besides, we observed an approximately fivefold decrease in mNG::ZYG-8 fluorescence on zygotic microtubules upon *zyg-8(RNAi)* (Figure S2E, F & H, Method M6). These genetic perturbations—loss of ZYG-8 from microtubules, overexpression, and partial depletion—provided the tools to investigate how different ZYG-8 levels affect mitotic spindle choreography.

Since ZYG-8 has been proposed to play a key role in spindle positioning, particularly during anaphase, we focussed on spindle pole oscillations occurring at this stage[57]. These oscillations have been widely used in previous studies to assess perturbations in spindle-positioning forces[58-60, 62, 63]. We quantified both the amplitude and frequency of the maximal oscillation at each spindle pole (Method M7). Following *zyg-8(RNAi)*, we observed a large increase in the amplitudes (Figure 1A-C) and a major decrease in the frequencies (Figure 1A, B & D). In *zyg-8(or484ts)* mutants at the restrictive temperature, oscillation amplitudes were further elevated (Figure 1C). Besides, oscillation frequencies at the anterior centrosome were also further decreased, while those at the posterior centrosome were more variable compared to other conditions – likely due to spindle misorientation – and therefore not significantly affected (Figure 1D). These results suggested that ZYG-8 acts to limit spindle oscillation amplitudes during anaphase. In embryos overexpressing *zyg-8*, maximal amplitudes remained unchanged (Figure 1C), but oscillation frequencies increased significantly (Figure 1D), indicating that oscillation frequency depends on ZYG-8 levels.

We and others have shown that the characteristics of spindle-pole oscillations were sensitive to microtubule dynamics[25, 63]. Besides, a previous study has investigated microtubule growth and nucleation perturbations in *C. elegans* zygotes across a broad range of MAP depletions, including ZYG-8[42]. This study found that ZYG-8 modestly promotes microtubule growth, and limits microtubule nucleation. To further explore these functions, we quantified both parameters in our three genetic perturbations. To assess whether the astral microtubule growth rate was altered, we used an EB-labelling of microtubule plus-ends (Method M8, Figure 2A). In *zyg-8(or484ts)* mutants at the restrictive temperature, we observed a significant 16% reduction in microtubule growth rate (Figure 2B), consistent with previous results using *zyg-8(RNAi)* by injection[42]. However, we detected no significant changes in growth rate in either *zyg-8(RNAi)* treated embryos or in those overexpressing *zyg-8* (Figure 2C, D). To test whether this modest reduction in microtubule growth could account for the exaggerated spindle-pole oscillations observed in *zyg-8* mutants, we performed a mild RNAi depletion of the ZYG-9^{XMAP215} microtubule polymerase[42, 75, 76]. As expected, this treatment resulted in a shorter mitotic spindle[75] (Figure S3A) and a reduced microtubule growth rate comparable to that measured in *zyg-8* mutants[42] (Figure S3B). However, spindle-pole oscillation amplitudes

and frequencies were either unaffected or slightly reduced by a mild *zyg-9* depletion, and did not phenocopy *zyg-8* mutant phenotype (Figure S3C, D). These results suggested that the modest role of ZYG-8 in promoting microtubule growth was not sufficient to account for its critical function in regulating spindle dynamics during anaphase.

Alternatively, ZYG-8 has been proposed to limit microtubule nucleation in the *C. elegans* zygote[42]. To test this, we estimated the nucleation rate of astral microtubules under our three genetic perturbation conditions. Specifically, we counted comet-like structures representing EBP-2::mKate2 labelled plus-ends of growing microtubules emanating from centrosomes (Method M8, Figure 3A). We observed a significant increase in the nucleation rate in *zyg-8(or484ts)* mutants and a decrease upon *zyg-8* overexpression, whereas *zyg-8(RNAi)* had no significant effect (Figure 3B-D). Since centrosome diameter correlates with nucleation capacity[77-79], we also measured centrosome size using mCherry::TBG-1 (Method M9, Figure 3E, F). We found a significant decrease in centrosome diameter upon *zyg-8* overexpression (Figure 3G), and a slight increase following *zyg-8(RNAi)* treatment (Figure 3H). These results collectively indicated that ZYG-8 functions to restrict microtubule nucleation. Next, we tested whether altered nucleation alone could explain the spindle-pole oscillation phenotype observed upon *zyg-8* perturbation. To this end, we partially depleted SPD-2^{CEP192} by RNAi to reduce microtubule nucleation[80] and assessed the effects on spindle pole oscillations. *spd-2(RNAi)* caused a marked reduction in centrosome diameter (Figure S4A, B). This perturbation was more pronounced than that seen with either *zyg-8* overexpression or RNAi. Concurrently, spindle-pole oscillation amplitudes were not significantly affected (Figure S4C). Unlike embryos overexpressing *zyg-8*, which showed reduced nucleation capacity and significantly increased oscillation frequencies, *spd-2(RNAi)* treated embryos exhibited either unchanged or only slightly decreased oscillation frequencies, despite showing a similar nucleation phenotype (Figure S4D). Together, these findings confirmed that ZYG-8 acts to limit microtubule nucleation rate, albeit modestly. However, this regulation alone did not account for the anaphase spindle oscillation phenotypes observed upon targeting *zyg-8*.

2- Cortical microtubule dynamics do not support a stabilization role for ZYG-8.

Previous works in human cells or *in vitro* have proposed that members of the Doublecortin family stabilises microtubules by preventing catastrophe and/or inhibiting depolymerisation[43, 81-83]. We investigated whether a similar regulation operates in *C. elegans* zygote. Inspired by a previous study on the role of CLS-2^{CLASP} in microtubule stability[84], we imaged embryos expressing GFP::TBB-2 or mCherry::tubulin at the cell cortex and examined both the number and duration of astral microtubule contacts there (Figure 4A, B; Movies S1-S4). If ZYG-8 limits depolymerisation or prevents microtubule catastrophe in the cytoplasm, we would expect a reduction in cortical contacts upon *zyg-8(RNAi)*. However, we observed the opposite: *zyg-8(RNAi)* resulted in an increased number of cortical contacts, while *zyg-8* overexpression led to fewer (Figure 4C, D). This finding contradicted the hypothesis that ZYG-8 stabilizes microtubules by preventing depolymerisation or catastrophe events within the cytoplasm. Next, to explore whether ZYG-8 could stabilize microtubules by reducing catastrophe frequency specifically at the cell cortex, we analyzed the duration of microtubule contacts. Surprisingly, *zyg-8(RNAi)* led to longer cortical residency times of astral microtubules, as reflected by a reduced frequency of short-duration contacts (Figure 4E, F). Conversely, *zyg-8* overexpression resulted in an increased frequency of shorter contacts, though the effect was

relatively modest (Figure 4G, H). Altogether, these measurements at the cell cortex did not support a role for ZYG-8 in stabilising microtubules.
To further test this finding, we examined spindle oscillation phenotypes following two distinct RNAi-mediated depletions. We depleted CLS-2^{CLASP}, a protein that stabilises microtubules by preventing catastrophe and promoting rescue[84, 85], and KLP-7^{MCAK}, a protein that destabilises microtubules by promoting their depolymerisation[86]. We validated the efficacy of each RNAi treatment by observing accelerated mitotic spindle elongation [87-89] (Figure S5A, D). Besides, mitotic spindle was longer during metaphase upon *klp-7(RNAi)*, as expected[90] (Figure S5D). *cls-2(RNAi)* treatment caused a slight increase in oscillation amplitudes and no significant variation in oscillation frequencies (Figure S5B, C). These phenotypes, resulting from microtubule destabilisation, were distinct from those observed upon *zyg-8(RNAi)*. It thus did not support a significant role for ZYG-8 in microtubule stabilisation. Conversely, KLP-7 depletion, which reduced microtubule depolymerisation, led to increased oscillation amplitudes at the posterior centrosome and decreased frequencies at both centrosomes (Figure S5E, F). If ZYG-8 stabilised microtubules by preventing their depolymerisation, we would have expected an oscillation phenotype opposite to that observed upon KLP-7 depletion. This was not the case. Thus, based on these comparisons, we concluded that ZYG-8 likely does not play a major role in stabilising microtubules.

Overall, we concluded that the perturbations of spindle-pole oscillations and microtubule dynamics at the cell cortex when we targeted *zyg-8* could not be explained solely by alterations in microtubule dynamics. Since proteins of the Doublecortin family have been proposed to regulate microtubule rigidity in neurons[34, 91], we asked whether the observed perturbations in spindle-pole oscillations and cortical microtubule behaviour could result from altered microtubule rigidity upon targeting *zyg-8*.

3- ZYG-8 would control microtubule flexural rigidity.

We first used the established agent-centred simulation *Cytosim*[92] to test whether variations in microtubule rigidity could affect microtubule dynamics at the cell cortex (Table S2, Method M11). We conducted three sets of simulations in which only the rigidity of astral microtubules was varied, set at 2, 10, and 25 pN.μm^2 (Movies S5-S7, Figure S6A). To assess whether these *in silico* changes in rigidity influenced microtubule curvatures, we calculated the local curvatures from fibre coordinates using a three-point method. We focussed on the 95th percentile curvature for each microtubule as a proxy for the highest curvatures (Figure S6B1). We observed that the highest curvatures increased as microtubule rigidity decreased (Figure S6B2). Then, we computed the tortuosity of astral microtubules (Figure S6C1) and found that lower rigidity led to increased tortuosity (Figure S6C2). Importantly, we also measured longer cortical lifetimes for microtubules with lower rigidity (Figure S6D). These results suggested that the increased proportion of microtubules with prolonged cortical contacts observed after *zyg-8(RNAi)* treatment may be due to a decrease in microtubule rigidity (Figure 4E). Therefore, the rise in instantaneous count of microtubule contacts at the cell cortex following *zyg-8(RNAi)* could result from a combination of increased microtubule nucleation and reduced flexural rigidity (Figure 4C).

Next, we explored the potential role of ZYG-8 in regulating microtubule flexural rigidity in the nematode zygote. To do so, we examined the shapes of the astral microtubules as a proxy for rigidity, following the same approach as in our *in-silico* experiments (Figure S6B, C) and as previously applied in studies of axonal growth cones[34]. In fixed embryos, we visualised

microtubules using immunostaining and confocal super-resolution microscopy (Method M3). In *zyg-8(RNAi)* treated fixed embryos, we observed more bent astral microtubules (Figure 5A). This phenotype was even more pronounced in *zyg-8(or484ts)* fixed mutants at the restrictive temperature, where microtubule curvatures were noticeably increased (Figure 6A). During anaphase, we also detected fragmented microtubules in the cytoplasm of some fixed mutant embryos (Figure 6A). Interestingly, such fragmentation may result from excessive curvatures, as previous studies have linked microtubule breakage to strong bending[93-95]. Earlier immunofluorescence images of *zyg-8* mutants showed very short astral microtubules[48, 72], a phenotype not fully explained by the modest reduction in microtubule growth rates (Figure 2). However, those earlier images were acquired from a single z-section, potentially missing longer, bent microtubules located in adjacent focal planes. Besides, fragmentation could also contribute to the appearance of shorter astral microtubules. In our fixed-embryo experiments, we observed this prominent phenotype of very-short astral-microtubule length in only a small subset of mutant embryos. To address the possibility of fixation-induced artifacts—especially considering that reduced microtubule rigidity might render them more fragile—we imaged live embryos expressing GFP::TBB-2 fluorescent labelling using a super-resolved confocal microscope (Nikon with Nsparc detector, Method M4). In *zyg-8(or484ts)* mutants, we were able to observe either long microtubules or sections of microtubules making contacts with the cortex (Figure S7A, Movies S8 & S9). These observations supported the conclusion that the moderate reduction in microtubule growth rate did not drastically affect microtubule length. Additionally, we observed regions of high local curvatures along astral microtubules, which appeared more frequent in the mutants (Figure S7A, Movies S4 and S5) compared to controls (Figure S7B and Movie S10). Unfortunately, the image quality in live embryos was limited due to the fast movement of the mitotic spindle, which required short exposure times. Besides, the high dynamics of the mitotic spindle and significant out-of-plane movement hindered visualisation of the full lengths of astral microtubules, particularly in *zyg-8(or484ts)* mutants (Movies S8 & S9). Consequently, we were unable to perform a reliable quantitative comparison of curvature phenotypes in live embryos.

To go beyond qualitative visual inspection, we set out to quantify the distribution of microtubule curvatures in fixed embryos. Direct measurements of microtubule rigidity in *C. elegans* embryos are not feasible with standard *in vitro* techniques (e.g., thermal fluctuations, optical trap/tweezers, or calibrated flow)[15-17, 32, 96-98]. As an alternative, previous studies have compared local curvature distributions as a proxy for rigidity[20, 95, 99]. Assuming that the forces acting on the microtubule network are similar between conditions, a higher proportion of strongly curved microtubules indicates reduced rigidity. This approach, however, requires accurate segmentation of microtubules, which is challenging due to their faint and uneven labelling. To address this, we assembled a five-step image processing pipeline that enabled segmentation of astral microtubules and computation of their local curvatures on a pixel-by-pixel basis using a three-point method (Figure S8, Method M12). By averaging curvature distributions across conditions, we observed a slight decrease in the proportion of low local curvatures following *zyg-8(RNAi)* treatment (Figure 5B, C). In *zyg-8(or484ts)* mutants at the restrictive temperature, the curvature distribution shifted significantly further toward higher values compared to controls, showing a stronger effect than RNAi (Figure 6B, C). Notably, some local curvature values reached up to 0.8 μm^{-1}, which were consistent with microtubule breakage events[93, 94]. To assess the highest curvatures, we calculated the 95th percentile curvature per microtubule and then extracted the median value per z-projected stack. We found slight increases following *zyg-8(RNAi)* (Figure 5D), and large and significant increases in

zyg-8(or484ts) mutants (Figure 6D). As a complementary measure of microtubule shape deformation—independent of curvature computation, which can be sensitive to sampling—we also quantified astral microtubule tortuosity[33]. We observed significantly greater tortuosity following *zyg-8(RNAi)* treatment (Figure 5E), and an even more pronounced increase in *zyg-8(or484ts)* mutants at the restrictive temperature (Figure 6E). Together, these analyses of astral microtubules demonstrated that ZYG-8 modulates microtubule curvature and tortuosity, supporting its role in regulating microtubule flexural rigidity.

4- ZYG-8 ensures spindle centring mostly by controlling microtubule rigidity.

Interestingly, the centring force generated by microtubules pushing against the cell cortex depends critically on microtubule rigidity[68]. Although this force was mostly invoked in metaphase[25, 27, 71], it is also thought to act as a restoring force for spindle rocking in anaphase[57, 60]. In *zyg-8(RNAi)* condition or in *zyg-8(or484ts)* mutants, we observed a large increase in the amplitudes of spindle pole oscillations (Figure 1C). We considered two possible and non-mutually exclusive explanations for this increase: enhanced cortical pulling or reduced cortical pushing.

First, we measured the most posterior position of the posterior centrosome during anaphase following *zyg-8(RNAi)* treatment and found no significant difference compared to controls (80.7 $\pm$ 1.4 % for *zyg-8(RNAi)* (N = 16), versus 79.8 $\pm$ 1.0 % for control embryos (N = 10), Student's t-test: p = 0.07)). This suggested that posterior displacement, driven by cortical pulling forces, remained largely unaltered. Next, we applied the DiLiPop analysis to assess cortical pulling and pushing events during anaphase, based on a statistical analysis of astral microtubule contact durations at the cortex[71] (Method M10). For pulling events, we observed a modest 10% rise in their lifetime (Figure 7A) and a slight 3% reduction in their density (Figure 7B). Since all cortical force generators are engaged in pulling events during anaphase, the reduced density following *zyg-8(RNAi)* likely reflected the prolonged duration of individual pulling events[63, 66]. We therefore concluded that *zyg-8(RNAi)* had only a modest effect on cortical pulling forces. In contrast, we found that pushing microtubules resided at the cortex significantly longer upon *zyg-8(RNAi)*, with a 37% increase in lifetimes (Figure 7C). This was consistent with their sensitivity to microtubule rigidity (Figure 7C). Besides, the density of pushing events increased by 22%, likely due to an elevated microtubule nucleation rate (Figure 7D). Despite the rise in pushing event density, we proposed that the larger oscillation amplitudes observed following *zyg-8(RNAi)* treatment resulted from a reduction in effective cortical pushing force. We attributed this reduction to decreased microtubule rigidity, which led to less efficient pushing events against the cell cortex.

To further investigate the role of ZYG-8 in modulating microtubule rigidity and the centering force generated by microtubules pushing against the cortex, we sought an alternative characterisation of spindle positioning forces at the cellular level. To do this, we extracted the mechanical fingerprint of spindle positional micro-movements along the transverse axis during anaphase and fitted a second-order model to the experimental spectrum[25] (Method M13). Our analysis revealed that ZYG-8 depletion caused a large 79% reduction in the centring-to-damping corner frequency f_c, compared to the control (Table 1). We also observed a 24% decrease in the diffusion coefficient D, which scales inversely with damping, and a 35% increase in the damping-to-inertia frequency f_0 (Table 1). We interpreted the decrease in f_c as primarily reflecting a centring force reduction due to softer microtubules[25]. The moderate decrease in D likely resulted from an increased number of microtubules contacting the cortex.

The rise in f_0 could be partly attributed to the reduced D, and appeared inconsistent with any notable increase in inertia, suggesting that the pulling forces were only mildly or not significantly affected. Overall, the mechanical fingerprint of spindle positioning following *zyg-8(RNAi)* treatment was qualitatively consistent with a reduction in the centring force, mainly due to softer microtubules. This reduction likely contributed to the increased amplitude of spindle pole oscillations.

In *zyg-8(or484ts)* mutants at the restrictive temperature, we observed larger amplitudes of spindle pole oscillation amplitudes compared to those seen with *zyg-8(RNAi)* treatment (Figure 1C). We hypothesized that this phenotype was due to a severely weakened centring force caused by excessively soft microtubules. This was supported by the increased proportion and magnitude of microtubule curvatures observed in these mutants (Figure 6). To test this hypothesis, we analysed spindle positional micro-movements in *zyg-8(or484ts)* mutants. We found a very large and significant reduction in the centring-to-damping corner frequency f_c, while the other two mechanical parameters, D and f_0, were not significantly altered (Table 1). These results suggested that in *zyg-8(or484ts)* mutants, the pronounced reduction in f_c, indicative of weakened centring forces, accounted for the exaggerated spindle pole oscillations. This reduction was likely due to decreased microtubule rigidity, consistent with the observed abnormalities in microtubule shapes.

To further support the role of microtubule rigidity in contributing to spindle centring, we targeted another protein known to regulate microtubule flexural rigidity in neurons to test whether similar perturbations in spindle choreography could be reproduced. We depleted PTL-1, the sole nematode homolog of the Tau protein family, using RNAi[100, 101]. This led to a modest increase in the maximal amplitudes of spindle pole oscillations and a decrease in their frequencies, both consistent with reduced microtubule rigidity (Figure S9). Besides, analysis of spindle positional micro-movements along the transverse axis during anaphase revealed a reduction in the centring-to-damping corner frequency f_c (Table 1). These results resembled those obtained with *zyg-8(RNAi),* suggesting a decrease in centring forces, though to a lesser degree. The milder phenotypes observed in *ptl-1(RNAi)* embryos were likely due to lower *ptl-1* expression levels in the zygote compared to *zyg-8*[102].

Altogether, our findings demonstrated that ZYG-8 regulated the cortical pushing force responsible for spindle centring, primarily by modulating microtubule flexural rigidity. This pushing force acted as a restoring force during anaphase spindle rocking. While cortical pulling forces remain the dominant drivers of spindle posterior displacement, our work highlighted the important, though often underappreciated, contribution of pushing forces to overall spindle choreography.

5- Very soft microtubules disrupt final spindle positioning and orientation.

Having identified an additional role for ZYG-8 in controlling microtubule flexural rigidity, we next investigated the importance of this function for successful asymetric mitosis. In *zyg-8(or484ts)* mutants at the restrictive temperature, the enhanced spindle-pole oscillation amplitudes – greater than those observed in *zyg-8(RNAi)* – resulted in a significantly reduced centrosome-to-cortex distance. We thus examined the consequences of this reduced distance in the course of anaphase. In untreated embryos, spindle oscillations gradually build up and then die down, ultimately leaving the spindle properly aligned along the anteroposterior (AP) axis of the embryo (Figure 8A). In contrast, in *zyg-8(or484ts)* mutants, the closer proximity of

the centrosome to the cell cortex pulled the entire spindle further toward the cell periphery. This appeared to prevent the spindle from re-centring during the oscillation die-down (Figure 8B). The reduction in cortical pushing disrupted the force balance, favouring excessive net pulling. As a result, the spindle failed to return to the central position by the end of anaphase, leading to both mispositioning and misorientation (Figure 8B-D). Notably, embryonic letality of *zyg-8(or484ts)* mutants was elevated (> 99%) at the restrictive temperature. Based on these observations, we proposed that the spindle misalignment seen in *zyg-8(or484ts)* mutants arose from impaired pushing forces, which disturbed the balance between pulling and pushing forces required for proper spindle positioning.

We hypothesised that reducing cortical pulling force could rescue the final spindle orientation in *zyg-8(or484ts)* mutants, by preventing an excessive imbalance between cortical pulling and pushing forces. To test this, we depleted GPR-1/2^{LGN} by RNAi. In wild-type *gpr-1/2(RNAi)* treated embryos, we observed no spindle pole oscillation and a most-posterior position of the spindle significantly shifted closer to cell centre, consistent with a decrease in cortical pulling forces (Figure S10A). Similarly, in *zyg-8(or484ts)* mutants treated with *gpr-1/2(RNAi)*, spindle pole oscillations were absent and the most-posterior position of the spindle was found closer to cell centre (Figure S10A). Strikingly, depleting GPR-1/2 in *zyg-8(or484ts)* mutants rescued the spindle mis-orientation defects (Figure S10B). This finding indicated that low microtubule rigidity did not affect final spindle orientation when cortical pulling forces were reduced. These results highlighted the critical importance of maintaining a proper balance between cortical pulling and pushing forces for accurate spindle positioning and successful cell division.

In conclusion, sufficiently rigid microtubules were required to generate the centring force necessary during anaphase, when cortical pulling forces are at their peak. This centring force prevented the centrosome from being displaced too far from the centre, ensuring proper final orientation of the spindle (Figure 8E). Reliable spindle positioning at the end of mitosis is crucial for accurate cleavage furrow placement during cytokinesis, a process that determines the proper partitioning of cell fate determinants[103].

DISCUSSION

Our work highlights a dual role for ZYG-8^{DCLK1} during mitosis, involving the control of both microtubule rigidity and dynamics. This conclusion is based on three distinct, complementary genetic perturbations of *zyg-8*. We confirmed previous findings by Srayko *et al.*, showing that ZYG-8 modestly promotes microtubule growth while limiting the nucleation of astral microtubules in *C. elegans* zygote[42] (Figures 2 and 3). Importantly, we propose that ZYG-8 plays a major role in *C. elegans* spindle choreography, primarily by rigidifying the microtubules. Indeed, the modest changes observed in astral microtubule dynamics in the cytoplasm upon targeting *zyg-8*, as well as its potential role in stabilising microtubules, are insufficient to explain the phenotypes related to spindle pole oscillations during anaphase or the altered behaviour of astral microtubule contacts at the cell cortex. This proposition is supported by multiple lines of evidence. If ZYG-8's main function were to stabilise microtubules by reducing their catastrophe rate at the cell cortex, *zyg-8(RNAi)* treatment would be expected to decrease the cortical lifetimes of astral microtubules, similar to what was observed with *cls-2(RNAi)*, where both cortical pulling and pushing event lifetimes were reduced[71]. In contrast, we found that *zyg-8(RNAi)* increases the lifetimes of cortical pushing events (Figure 7A, C). This result also argues against a major role for ZYG-8 in preventing microtubule depolymerisation.

Indeed, upon *klp-7(RNAi)*, which reduces microtubule depolymerisation, we previously observed a specific increase in pulling event lifetimes[71]. Similarly, if ZYG-8 primarily promoted microtubule growth, *zyg-8(RNAi)* should result in fewer astral microtubules reaching the cortex and shorter contact durations, as previously seen with *zyg-9(RNAi)*[71]. Instead, in our current study, we observe the opposite phenotypes (Figure 4C, E-F). Furthermore, if ZYG-8 limited microtubule catastrophe within the cytoplasm, then *zyg-8(RNAi)* would be expected to decrease the number of astral microtubule contacts at the cell cortex, as more microtubules would depolymerise before reaching it. This, again, contradicts our observations (Figure 4E). By contrast, the increased number of astral microtubule contacts upon *zyg-8(RNAi)* aligns with a role for ZYG-8 in limiting microtubule nucleation. However, this effect alone, which is moderate compared to nucleation perturbation upon targeting *spd-2*, cannot fully account for the observed variations in microtubule cortical-contact number. We propose that ZYG-8 also regulates microtubule rigidity, and that this additional function helps explain the phenotype. Less rigid microtubules that grow against the cortex are more likely to bend, which reduces the cortical pushing force. As a result, this bending delays catastrophe onset and increases cortical contact lifetimes. Thus, the increased instantaneous number of astral microtubule contacts observed upon *zyg-8(RNAi)* likely results from a combination of enhanced nucleation and prolonged pushing event durations due to reduced microtubule rigidity. Interestingly, the altered frequency of spindle pole oscillations upon targeting *zyg-8* is consistent with a role in modulating microtubule rigidity, rather than with its previously reported function in limiting microtubule nucleation[57, 68] (Figure 1D). This proposition is further supported by observed changes in microtubule shape in *zyg-8(RNAi)* treated embryos and in *zyg-8(or484ts)* mutants (Figures 5 and 6). Why ZYG-8 plays a greater role in regulating microtubule rigidity rather than microtubule dynamics. This is likely because ZYG-8 and EB compete for the same microtubule binding site at the corner of four tubulin dimers[36, 104, 105]. However, EB binds preferentially to the GTP cap at growing ends[104], while Doublecortin-family proteins bind *in vitro* to the whole lattice[106]. *In vivo*, DCX was excluded from microtubule ends[107]. An exclusion of ZYG-8 from microtubule ends in *C. elegans* zygote could account for the efficiency differences in its dual role. This dual role may be particularly relevant in specific cellular contexts where proteins essential for microtubule growth or nucleation (e.g., γ-tubulin ring complexes) are absent or present at low levels. In line with this, previous studies have shown that γ-tubulin-independent mechanisms for microtubule nucleation do exist[108, 109]. Interestingly, proteins from the Doublecortin family are highly expressed in neurons, where they regulate microtubule rigidity[34, 91]. They may also contribute there to microtubule nucleation and/or growth, consistent with their *in vitro* capabilities[35, 82, 83, 110]. Collateral branching in hippocampal neurons was significantly delayed following DCX depletion, which may reflect microtubule dynamics impairment[111]. Overall, ZYG-8^{DCLK1} performs multiple microtubule-related functions in a context-dependent manner; we suggest controlling flexural rigidity as a novel one during cell division and possibly beyond.

Looking ahead, it will be important to explore the mechanisms by which ZYG-8 rigidifies the microtubules. Several mechanisms have been proposed, primarily in the context of neurons. Here, we draw on the body of research on the DCX protein, which shares the same two microtubule-binding domains as DCLK1^{ZYG-8}. Besides, these two doublecortin domains are highly conserved in ZYG-8[48]. (1) Microtubules can be rigidified by hindering the sliding of protofilaments through the binding of MAPs across these protofilaments. DCX binding on the microtubules is compatible with this mechanism since it reinforces lateral and longitudinal dimer couplings[35]. (2) Rigidification can also occur by bundling multiple microtubules together.

Previous studies revealed such a mechanism for the Doublecortin family *in vitro* and *in vivo*[51, 81, 82, 91, 110, 112, 113]. In particular, *zyg-8(or484ts)* mutants displayed a perturbed bundle organisation of microtubules in touch receptor neurons[91]. However, in the *C. elegans* zygote, electron microscopy failed to reveal microtubule bundles in the spindle or astral microtubules close to the poles[114]. Therefore, we disfavoured such a mechanism. (3) Microtubule rigidity is also regulated through post-translational modifications (PTM)[115-119]. Notably, a study showed that DCX expression increases tubulin polyglutamylation in neurons [120]. However, the *ttll-4(-);ttll-5(-);ttll-11(-)* triple mutants, which prevented tubulin glutamylation, did not show any defect in embryonic viability. It suggested that microtubule glutamylation may not significantly affect the zygote cell division[121]. (4) It was previously shown that damages along microtubule lattice soften microtubules[122, 123]. Thus, self-repair of local damages may also help restore the rigidity or stabilise the curved region[124]. Interestingly, the number of microtubule defects could notably correlate with the microtubule growth rate[125, 126]. The latter is particularly high in nematodes[127]. If a high occurrence of holes exists in the *C. elegans* embryo, ZYG-8 could contribute to healing as the Doublecortin family also acts as tubulin oligomer chaperones[83]. However, to date, there has been no evidence of microtubule lattice defects in *C. elegans* zygote. For example, embryos with EBP-2 fluorescent labelling did not show stationary fluorescent spots along the astral microtubules[42, 58]. The various mechanisms proposed above, in which ZYG-8 could play a key role in regulating microtubule flexural rigidity, are not mutually exclusive; several of them may be combined. ZYG-8 rigidifying the microtubule by coupling the protofilaments appears to us the most plausible mechanism currently.

Focussing on mitotic spindle positioning in the *C. elegans* zygote, the current study both complements and departs from previous investigations**.** Firstly, we show that controlling microtubule flexural rigidity participates in the spindle choreography. In particular, this control helps prevent the spindle poles from approaching the cell periphery too closely during anaphase (Figure 8A, B, E). Consistently, we observed increased amplitudes of spindle pole oscillations following ZYG-8 or PTL-1 depletion (Figures 1C & S9A). This control through microtubule rigidity is complementary to the well-established regulation involving microtubule dynamics[25, 58, 63, 71]. Secondly, our study underlines that cortical pushing force contributes to spindle positioning during anaphase, though in a manner distinct from that of cortical pulling forces. Cortical pulling forces are dominant, and their asymmetry, controlled by PAR polarity, ensures spindle posterior displacement[65, 69, 89, 128-130]. To date, cortical pushing forces have been proposed to contribute to spindle centring during metaphase[25, 27]. During anaphase, although restoring forces are known to be necessary for spindle oscillations, the role of cortical pushing force as restoring force was not demonstrated[57]. Besides, it is often assumed that cortical pushing force plays a minimal role during anaphase, due to the high magnitude of cortical pulling forces and the dampening effect of microtubule buckling[59, 70, 131]. However, we propose that weakening the cortical pushing forces, as observed in *zyg-8(or484ts)* mutants, hinders spindle alignment along the AP axis (Figure 8B). This force imbalance compromises the final position and orientation of the spindle (Figure 8C-D). Interestingly, decreasing cortical pulling force by depleting GPR-1/2 in *zyg-8(or484ts)* mutants rescues the spindle misorientation phenotype (Figure S10). Together, these findings highlight the importance of sufficiently strong cortical pushing forces during anaphase, which contribute to proper force balance and ensure accurate spindle orientation at the end of mitosis. Thirdly, we show that in *zyg-8(or484ts)* mutants, astral microtubules are still able to contact the opposite cortex (Figure S7A, Movies S8 and S9). This rules out a model in which spindle misorientation arises from a failure of microtubules to reach the cortex, as previously

suggested[48]. Moreover, our interpretation differs from that of Kozlowski *et al*., who suggested that limited access of astral microtubules to the cell cortex causes spindle oscillation[58]. Overall, the astral microtubule network functions like a spring, restricting the spindle transverse motion away from the centre in *C. elegans* zygotes[25, 27, 68]. From this perspective, microtubule flexural rigidity emerges as a key physical parameter controlling the magnitude of centring forces. This mechanical contribution is essential for generating cortical pushing forces strong enough to counteract the intense cortical pulling forces that act during anaphase.

We foresee that the essential role for pushing goes beyond the nematode's first division and may be relevant to other asymmetric divisions and maybe further. It is well established that the pulling dominates the spindle orientation. It is accounted for by the canonical model based on the molecular machinery composed of the cortical Gα-LGN^{GPR}-NuMA^{LIN-5} complex and the cytoplasmic dynein motor[10, 132]. However, less attention has been paid to the contribution of the pushing forces to spindle orientation. The dependence of spindle orientation on cell shape, which is often neglected, suggests that the pushing force could play a significant role in this process[133-137]. In other systems, some studies found that the spindle did not align with the dynein-enriched cortical zones[138-141]. Consequently, the traditional canonical model alone cannot account for spindle orientation in various contexts. We propose that the cortical pushing force contributes to this phenomenon and that the flexural rigidity of microtubules must be sufficiently high. Notably, the orientation of the mitotic spindle defines the direction in which a cell divides. Therefore, many developmental processes, ranging from germline stem cell division to epithelial tissue homeostasis and regeneration, require correct mitotic spindle orientation. Defects in spindle orientation have been associated with various diseases, such as organogenesis and morphogenesis failures, or cancer[142-149].

By uncovering ZYG-8's dual role in *C. elegans* mitosis, we can now question its contribution to zygote meiosis, especially through controlling microtubule flexural rigidity. A recent study highlighted that ZYG-8 promotes meiotic spindle stability and suggested that it may regulate microtubule dynamics and motor-driven forces[50]. We wonder whether some of the perturbations that they observed upon targeting *zyg-8* could be attributed to the deregulation of microtubule rigidity. Notably, they found that most *zyg-8(or484ts)* meiotic spindles were significantly bent at the restrictive temperature. Additionally, some images of the mutant showed microtubules exhibiting high local curvatures. Similar perturbations were also observed following ZYG-8 depletion using the Auxin-inducible degradation system. In light of these observations, it is plausible that ZYG-8 contributes to the assembly or/and stability of meiotic spindles in the zygote by stiffening microtubules.

In conclusion, our findings regarding the pivotal role of ZYG-8^{DCLK1} in spindle positioning and orientation, primarily through rigidifying microtubules during mitosis offer not only a deeper understanding of the fundamental mechanisms governing cell division but also highlight significant implications for cancer therapy. Given that DCLK1^{ZYG-8} is frequently deregulated in various solid tumours (e.g., those from the colon, pancreas, kidney and breast), this suggests its involvement in a common process such as cell division[150-153]. Additionally, as the proteins of the Tau family are also found to be deregulated or mutated in cancers, targeting microtubule rigidity may represent a promising approach for future cancer treatments[154-156]. This strategy could potentialise existing therapies targeting microtubule dynamics, which often suffer from side effects and are limited by cancer cell resistance.

MATERIAL AND METHODS

M1- C. elegans strains and their culturing

The *C. elegans* strains used in the present study are listed in Table S1. *C. elegans* nematodes were cultured as described in [157] and dissected to obtain embryos. The strains were maintained at 20°C, except the thermosensitive mutant *zyg-8(or484ts)* maintained at 15°C and AZ244 maintained at 25°C to increase transgene expression. The strains were handled on nematode growth medium (NGM) plates and fed with OP50 *E. coli* bacteria.

M2- RNAi feeding

RNA interference (RNAi) experiments were performed by feeding, as described in [158]. Bacteria were obtained by Source BioScience (*zyg-8*: III-6C10; *ptl-1*: III-1A12; *spd-2*: I-4O08; *zyg-9*: II-6M11; *cls-2*: III-4J10; *klp-7*: III-5B24; *gpr-1/2*: III-4J09). The feedings were performed at 20°C, except for *gpr-1/2* realised at 15°C to be at the restrictive temperature of *zyg-8(or484ts)* mutant. For RNAi targeting of *gpr-1/2, zyg-8* and *ptl-1*, the treatment lasted 96 hours and dsRNA expression was induced with 4 mM of IPTG (Isopropyl β-D-1-thiogalactopyranoside). For *spd-2*, *zyg-9*, *klp-7* and *cls-2*, dsRNA expression was induced with 3 mM IPTG. The RNAi treatment duration was 6 hours for *zyg-9* and *spd-2*, 24 hours for *klp-7*, and 48 hours for *cls-2*. The control embryos for the RNAi experiments were fed with bacteria carrying the empty plasmid L4440.

M3- Preparation of the embryos for live imaging or immunofluorescence

For live imaging, embryos were dissected in M9 buffer (prepared by combining 3 g KH_2PO_4, 6 g Na_2HPO4, 5 g NaCl and 1 mL of 1 M $MgSO_4$ diluted in ultrapure water to 1 L) and mounted on a pad (2% w/v agarose, 0.6% w/v NaCl, 4% w/v sucrose) between a slide and a coverslip.
For immunofluorescence staining, embryos were dissected in M9 buffer and mounted on a slide coated with poly-L-lysine (0.1%) (Sigma-Aldrich P1524). The slides were dipped in liquid nitrogen to crack the embryo's eggshell and immediately transferred to -20°C methanol for fixation for 20 minutes (freeze-cracking method[159]). They were then rinsed for 10 minutes in PBS 1X before blocking for 20 minutes in PBS-Tween (0.2%) with BSA (1%).
Importantly, for the thermosensitive *zyg-8(or484ts)* mutants, we transferred them as L4 larvae to 25°C and incubated for 15 hours before use, as previously done in [48].

M4- Fluorescence microscopic imaging conditions

The various microscopy setups used are presented in the table below. Embryos were imaged at 23°C, except otherwise stated. Images were stored using the Omero software[160].

Imaging experiment	**Spindle pole imaging**	**(1) Landing assay to study microtubule cortical contacts; (2) Microtubule dynamics (growth and nucleation rates)**	**(3) Microtubule network; (4) ZYG-8 localisation inside the embryo**	**(5) Microtubule live imaging**
Live or fixed embryo	Live	Live	(3) & (4): Fixed	Live
Microscope type	Zeiss Axio Imager upright	Leica DMi8 equipped with CSU-X1 spinning disk head (Yokogawa)	(3) & (4): Airyscan 2 Zeiss LSM980.	Nikon AX

Fluorescent labelling	Spindle poles, e.g. mCherry::TBG-1	(1) Microtubules: GFP::TBB-2 or mCherry::tubulin. (2) Microtubule plus-ends : EBP-2::mKate2	(3) DM1A-AF488 conjugate. (4) mNG::ZYG-8 and mCherry:tubulin.	GFP::TBB-2
Objective	100x/1.45 NA Oil plan-Apo	100x/1.4 NA Oil HCX Plan Apo	63x/1.4 NA Oil Apochromat DIC M27	63x/1.42 Oil Plan Apo OFN25 DIC N2
Acquisition plane(s)	Spindle plane	(1) Cortex plane close to the glass slide (located 12-15 µm below the spindle plane). (2) For *zyg-8(RNAi)*: spindle plane; for *zyg-8* overexp. and *zyg-8(or484ts)*: ~3 µm below spindle plane	(3) 25-30 or (4) 10-12 z-sections centred at the spindle plane; z-step: (3) 0.17 µm, (4) 0.3 µm.	Spindle plane
Camera / detector	Andor iXon3 EMCCD 512x512	ultra-sensitive Roper Evolve EMCCD	Airyscan detector	Nikon NSPARC detector
Illumination, excitation and emission characteristics	Illumination: mercury lamp. NG channel: excitation: enhanced transmission (ET) 485/12 bandpass (BP) (AHF analysentechnik); beamsplitter: low pass (LP) 495; emission: 525/50 ET Bandpass mCherry channel: excitation: BP 530-585; beamsplitter: 600; emission: low pass 615	Illumination: Argon laser mCherry channel: laser selecting the line at 561 nm with DAPI-GFP-mCherry-Cy5 emission filter and a Quad Dichroic filter. GFP channel: laser selecting the line at 488 nm with GFP/FITC 4 nm BP excitation filter and retrieving fluorescence with a Quad Dichroic emission filter	Illumination: laser diodes (3) excitation wavelength 488 nm; main beam splitter (MBS) 488/639 and 405. (4) excitation wavelength 488 nm or 561 nm; MBS 488/561 and 405; secondary beam splitter LP525 (for 488 nm laser) or SP550 (for 561 nm laser).	Illumination: laser excitation wavelength 488 nm ; Emission filter 502-546 nm.
Spatial resolution (µm/pixel)	0.16	0.14	(3) & (4): 0.04.	0.115
Temporal resolution	32.498 frame/s	(1) 10 frame/s (2) 2.5 frame/s	(3) 41.6 s per frame (4) 1 min 23 s per frame	1.962 s per frame
Additional parameters or equipment	Extra anti-heat and ultraviolet filters added to the mercury lamp light path for long-term time-lapse	Adaptive Focus Control (AFC, Leica)	Mode: (3) & (4): Super Resolution. Averaging: (3): line, number: 2 lines, method: mean; (4) none.	Mode: Galvano unidirectional; Super resolution Integrating: 2 Dwell time: 2 µs
Post-processing	None	None	Deconvolution	None

Software	Andor Solis (Oxford instruments)	Imaging Solution (Inscoper, SAS)	ZEN blue (Zeiss)	NIS-Elements AR

M5- Localisation of ZYG-8 in the C. elegans one-cell embryo

To study ZYG-8 localisation in the zygote, we used *C. elegans* strains expressing fluorescently labelled microtubules (mCherry::tubulin) and fluorescently labelled ZYG-8 (mNG::ZYG-8) (Figures S1A-C and S1G-I). We analysed deconvolved dual-colour images of fixed embryos acquired using the Zeiss Airyscan 2 microscope. First, we computed the intensity profiles of both mCherry::tubulin and mNG::ZYG-8 signals along a 5-pixel wide line (Figures S1D-E, J-K). The lines used for this analysis are shown in Figure S1D, J. Co-localisation of intensity peaks indicated the binding of ZYG-8 to microtubules. Second, we investigated pixel-wise co-localisation by producing a scatterplot and computed Pearson's correlation coefficient *r* (Figure S1F, L). Statistical significance was assessed through the Costes statistical test using 200 rounds of randomisation and a bin width of 0.001[161]. These analyses were performed using Fiji and the JACoP plugin[162].

M6- Quantification of ZYG-8 level at the worm and embryo scales

To quantify the ZYG-8 level at the worm scale, we performed a Western blot analysis using protein extracts obtained from different *C. elegans* strains (Figure S2A-B). For each experiment, 30 adult hermaphrodites were picked into 200 µL of M9 buffer and snap-frozen in liquid nitrogen, then thawed, mixed with 6.5 µL loading buffer (DTT 0.1 M), and loaded onto a Mini Protean TGX 4–20% Tris-Glicine gel from Bio-Rad (Hercules, CA). Immunoblots were probed using the primary anti-OLLAS antibody (Novus Biologicals NBP1-06713, 1 mg/mL, host: rat) diluted at 1/2000 and the primary anti-tubulin antibody (Sigma-Aldrich T5168, host: mouse) diluted at 1/2000, and then revealed using an HRP (horseradish peroxidase) conjugated secondary antibody (1:20000; Jackson ImmunoResearch, West Grove, PA; host: rat for antiOLLAS & mouse for anti-tubulin). Membrane saturation and all antibody dilutions were made in PBS–Tween 0.2% and 5% non-fat dry milk. Blots were incubated with WesternBright ECL spray (Advansta K-12049-D50) before detecting by chemiluminescence on an Amersham Imager 680 (GeHealthcare, Chicago, IL). Quantification was performed using Fiji[163].

To complement the first quantification, we analysed deconvolved dual-colour images of embryos carrying two fluorescent tags: mCherry::tubulin and mNG::ZYG-8. For each embryo, we realised, in the same regions of interest (ROI), red and green fluorescence intensity measurements (mean within ROIs) using Fiji: 2 square ROIs (40 x 40 pixels; 1.6 x 1.6 µm) within the spindle (1 per half-spindle), 3 square ROIs (40 x 40 pixels) within the cytoplasm, 5 curvilinear ROIs on astral microtubules using the segmented line tool, and a ROI (40 x 40 pixels) outside the embryo, the latter to measure the background fluorescence. Exemplar ROIs are highlighted in Figure S2C. For spindle and cytoplasm measurements, fluorescence quantification was performed on maximum projected images (3 z-sections centred on the spindle mid-plane). After subtracting the background fluorescence (mean intensity in corresponding ROI) from each fluorescence of interest (spindle, cytoplasm and astral microtubule) and for each channel separately, we computed the ratio of ZYG-8 fluorescence over tubulin fluorescence for the three measurements (Figure S2G, H).

M7 - Centrosome-tracking assay and oscillation characterisation

The tracking of labelled centrosomes (e.g., mCherry::TBG-1) and the analysis of their trajectories were conducted using custom tracking software developed using Matlab (The MathWorks)[57]. Tracking of γ-tubulin labelled embryos fixed in -20°C methanol demonstrated an accuracy of 10 nm[25]. To determine embryo orientations and centres, we performed cross-correlation of the embryo background cytoplasmic fluorescence with artificial binary images that represented an embryo. We calculated the embryo size (lengths of the long and short axes) using the active contour algorithm[164]. From the spindle pole positions, we measured the maximal amplitudes of anaphase oscillations (peak-to-peak) for both poles, normalised to the length of embryo's short axis, as well as the frequencies of these maximal oscillations (e.g., Figure 1). We also assessed mitotic spindle length, normalised to the length of embryo's long axis, and the maximal spindle elongation rate following nuclear envelope breakdown (e.g., Figure S5D). Finally, we quantified the spindle position (the midpoint between the two centrosomes), and the spindle orientation (the angle between the spindle axis and the embryo's long axis) at the end of mitosis, specifically at 150 s after the anaphase onset (e.g., Figure 8C-D).

M8 - Characterisation of astral microtubule growing and nucleation rates

We labelled microtubule plus-ends using EBP-2::mKate2, which form comet-like structures as the microtubules grow (Figures 2A and 3A). We performed an analysis of the comets adapted from the article by Srayko *et al.* using Fiji (except otherwise cited)[42]. We measured microtubule dynamics during metaphase.

To measure the growth rates, we first denoised the movies using Kalman filtering, with the gain set to 0.5 and the initial noise estimate set to 0.05[165] (Figure 2A). Next, we traced a line along the comet trajectory in the pre-processed movie, restricting to comets that remained visible for at least 10 frames (4 s). We generated a kymograph from the traced line to assess comet displacement velocity. We repeated the measurement approximately 50 times for each condition across about ten embryos (about 25 comets per centrosome).

To measure the nucleation rate, we first denoised the movies using Candle filtering (parameters: *beta* = 0.1; *patchRadius* = 1; *searchRadius* = 3; *back* = 1) (Figure 3A). We did not apply additional pre-processing for *zyg-8(RNAi)* treatment, *zyg-8* overexpression and their control. However, for *zyg-8(or484ts)* mutants and untreated embryos, we enhanced contrast using an unsharp mask (*radius* = 1; *Mask weight* = 0.7). Since centrosomes moved during metaphase, we applied Icy's rigid registration plugin (v1.4) on the denoised images[166]. This registration aligns each image with a reference image to correct for centrosome displacements, as described in[167]. Doing so, we accurately counted the comets crossing a half-circle region of interest (ROI) positioned 9 µm from the centrosome after [42]. We generated kymographs over 150 frames (60 seconds). To address the inhomogeneous background in the raw kymographs, we applied background subtraction using Gaussian blurring. We then set an intensity threshold to retain the brightest 2% of pixels in *zyg-8(RNAi)* and control kymographs, and 2.5% for *zyg-8* overexpression ones, *zyg-8(or484ts)*, and their controls. Finally, we used the "Analyze particles" command and counted objects considered as individual EBP-2 comets (particle size: 2 pixels to infinity, 0.14 µm/pixel). Measurements were done for both anterior and posterior centrosomes, except when only a single centrosome was clearly visible.

M9 - Centrosome-size measurements

We analysed images of embryos labelled with either mCherry::TBG-1 and mCherry::HIS-58, or GFP::TBG-1 and GFP::HIS-11, by tracking their centrosomes (cf. M7). Based on the tracked

positions, we extracted vignettes of 6.4 x 6.4 µm (40 x 40 pixels; Figure 3E, F). We then performed a 2D Gaussian least-square fit to characterise both the posterior and anterior centrosomes every second [168]. From these fits, we obtained the *x*- and *y*-widths and calculated the diameter of the centrosomes, assuming they are round, using the formula: $D = \sqrt{x^2 + y^2}$.

M10 - Landing assay to study astral microtubule cortical contacts

The entire microtubule lattices were fluorescently labelled using GFP::TBB-2 or mCherry::tubulin to view them in all their states. We used the same approach as the one previously implemented in [71] and available on Zenodo (doi: 10.5281/zenodo.4552485); we combined a Kalman filtering[165] (gain set to 0.5 and initial noise to 0.05) and *u-track* [169] whose parameters are listed in the table below. Movies S1–S4 show representative examples of microtubule contact tracking under the four conditions we studied. After tracking the microtubule contacts, we quantified the number of microtubule cortical contacts per frame, averaged the values over a 10-second window, and normalised them by the embryo area. This provided an instantaneous count of microtubule contacts throughout mitosis for each embryo, which we then averaged across embryos within each experimental condition (e.g., Figure 4C). We also computed the duration histograms of astral microtubule contacts per embryo and averaged these histograms across embryos for each condition (e.g., Figure 4E).
We then performed the DiLiPop analysis. This statistical analysis of the microtubule cortical contact durations reveals the short-lived and long-lived populations of astral microtubules at the cortex associated with pulling and pushing events, respectively[71]. By globally fitting the embryo-set duration distributions of a given condition, we obtained the characteristic lifetimes and densities of the cortical pulling and pushing events (e.g., Figure 7). Error bars of the lifetimes and densities were obtained by bootstrapping as explained in [71]. These densities of events are distinct from instantaneous contact density and thus independent of the cortical contact durations (except in the case of anaphase pulling events due to all force generators being involved in pulling).

u-track step	**Parameter name**	**Parameter value**
Detection	Gaussian standard deviation	1.2
	Alpha-value for initial detection of local maxima	0.14* / 0.12**
	Rolling window time-averaging	3
	Iterative Gaussian mixture-model fitting	0
Tracking	Maximum gap to close	5
	Merge split	0
	Minimum length of track segments from the first step	1
Cost function frame-to-frame linking	Flag for linear motion	1
	Allow instantaneous direction reversal	1
	Search radius lower limit	1
	Search radius upper limit	3
	Standard deviation multiplication factor	3
	Nearest neighbour distance calculation	1
	Number of frames for nearest neighbour distance calculation	4
Cost function close gaps	Flag for linear motion	1
	Search radius lower limit	1
	Search radius upper limit	3

	Standard deviation multiplication factor	3
Nearest neighbour distance calculation	Number of frames for nearest neighbour	4
	Penalty for increasing gap length	1.5
	Maximum angle between linear tracks segments	30

* for GFP::TBB-2 labelling; ** for mCherry::tubulin labelling.

M11 - Simulation using Cytosim

We used *Cytosim* to simulate cytoskeletal filaments[92]. We modified *Cytosim* to allow multiple fibre types to emanate from a single aster and to exert a given external force on solids, fibres or spheres (doi: 10.5281/zenodo.14246919). We conducted a 2D simulation of the first mitosis of the *C. elegans* zygote, focusing on spindle positioning and the astral microtubule network (Figure S6A). The simulation represented the spindle as a rigid rod implemented with static spindle microtubules, excluding any dynamic elements such as motor proteins. The parameters used in the simulation are detailed in Table S2 and the simulation files are provided as supplemental files S1, S2 and S3 with an exemplar video for each microtubule rigidity (Movies S5-S7). Importantly, to mimic cortical asymmetric pulling forces, we applied external forces at the spindle poles: -180 pN at the anterior pole and +300 pN at the posterior pole[69]. We attached two types of fibres to each solid, which simulated the centrosomes, to differentiate between spindle and astral microtubules. The astral microtubules were defined as fibres without dynamics at their minus ends and with plus-ends displaying classic dynamic instability. We set their total number to 75, according to our estimated count of astral microtubules longer than about 2 µm in a 2D plane. Their rigidities were varied at 2, 10, or 25 pN·µm², reflecting the range of *in vitro* measurements[21], with these differences allowing for visible variations in microtubule curvatures. Additionally, these fibres could engage with cortical force generators simulated as hands bound to the cortex.

We measured both the highest curvatures (95th percentile) and the tortuosity of the astral microtubules (Figure S6B-C) after 45 seconds of simulation, following the approach outlined in method M12.

To estimate the durations of fibre cortical contacts, we analysed fibre lengths, end positions, and cortical anchor positions. When microtubules push against the cortex, they grow slowly due to the force-velocity relationship, remaining near the cell cortex. We first tracked fibre lengths over time to identify instances of very low growth rates (under 0.18 µm/s), indicating moments when the fibres were stalled (neither growing nor shrinking). Next, we calculated the distances between fibre end positions and cortical anchor (hand) positions during these stalling events to identify the events whose distance was below 1 µm. Over 45 seconds (beginning 15 seconds after the simulation started to allow for warm-up), we recorded the durations of fibre cortical contacts and constructed the corresponding histogram. We then fitted it with a mono-exponential model[58, 170]. This analysis yielded a characteristic lifetime for each simulation run (Figure S6D).

M12 - Mapping astral microtubules and characterising their local curvatures and their tortuosity

We stained microtubules using an anti-α-tubulin antibody, clone DM1A raised in mouse, Alexa Fluor® 488 conjugate (Sigma-Aldrich 16-232), diluted at 1/500 in PBS-Tween (0.2%) with BSA (1%). It targets several α-tubulin isoforms in various species. Antibody incubation was performed overnight at 4°C. Slides were then rinsed for 10 minutes in PBS-Tween (0.2%),

twice, in a light-free environment. We could then visualise microtubules all along their length. We identified the z-section(s) as the more appropriate for astral microtubule segmentation. For most embryos, we found a single z-section per embryo for which both centrosome asters were visible. For some embryos having the two centrosomes on distinct z-sections, we considered two planes of interest.

Five-step image processing pipeline to map the local curvatures of the astral microtubules (Figure S8A). **(1)** We used the planes above and below the plane of interest to perform an extended depth of field projecting the 3 z-sections into a single image (Figure S8B) [171]. We thus better visualise microtubules all along their length. **(2)** We applied the *Orientation Filter Transform* (OFT, number of orientations = 20; radius = 5 pixels) since it is effective in enhancing filamentous pattern against noises[20, 172] (Figure S8C). **(3)** We then used the interactive machine-learning tool, *Ilastik,* to segment the astral microtubules (Figure S8D). The dedicated paragraph below provides more detailed information about our segmentation. **(4)** We generated the skeleton of the filament traces from the binary segmentation, taking advantage of *SOAX* (Figure S8E). Further information about the use of SOAX is available in a dedicated paragraph below. **(5)** We finally measured the local curvatures of astral microtubules pixel-by-pixel from the skeleton coordinates, enabling mapping of the local curvatures (Figure S8F). For a set of three neighbouring points sampling the curve, the local curvature corresponds to the inverse of the radius of the circle going through the mid-point and best fitting the two others. Local curvatures were computed along microtubules according to the three-point method[173] using a code retrieved on Matlab Central[174]. In a nutshell, microtubules are viewed as parametrised curves; at each point, the *x* and *y* coordinates are represented as second-order polynomials of the curvilinear abscissa passing through the point and its two neighbours. The curvature is then computed with the Frenet-Serret formula.

Ilastik: We initially trained *Ilastik* using the conditions *zyg-8(RNAi)* and its control during metaphase. This involved approximately 10 manual annotations of microtubules across three embryos for each condition to cover various intensities, contrasts and microtubule shapes. We then used this trained model, referred to as #1M (M for metaphase), to segment, in a semi-supervised way, the astral microtubules in metaphase images. Next, we trained the model to segment anaphase images of *zyg-8(RNAi)* treated embryos and their controls. Indeed, denser microtubule networks in anaphase required additional annotations. This led to the upgraded model #1A that we used to segment anaphase images. We then analysed *zyg-8(or484ts)* mutants and untreated embryos in metaphase. The model was further improved by manually annotating three mutants, resulting in model #2M, which we used to segment images of both mutants and untreated embryos in metaphase. We applied a similar process for segmenting anaphase images of mutants and untreated embryos, enhancing model #2M with a few annotations of anaphase mutants to get the model #2A. The table below summarised the *Ilastik* models used to produce the data displayed in the different figures.

***Ilastik* model**	**Used for data displayed in figures**
#1M	5B; 5D & 5E (only metaphase)
#1A	5C; 5D & 5E (only anaphase)
#2M	6B; 6D & 6E (only metaphase)
#2A	6C; 6D & 6E (only anaphase)

SOAX: We extracted the centrelines from the thick filaments utilising SOAX mostly with standard parameters. We made the few specific adjustments highlighted in the table below. These five adjusted parameters were crucial for accurately delineating the curved regions of the microtubules. The settings used ensured that the centrelines faithfully represented the shapes of the microtubules, as confirmed through visual validation. Additionally, manual corrections could be applied at this stage, especially when two microtubules were mistakenly merged into one.

***SOAX* parameter name**	**Parameter value**
Snake Point Spacing	4
Beta	0.01
Stretch Factor (k_str)	0.8
Radial Near (pixels)	8
Radial Far (pixels)	16

Microtubule shape quantification: We analysed only the astral microtubules that were at least 4 μm long after segmentation, as shorter ones often represented fragments. This approach was appropriate for comparing conditions without seeking absolute quantification. We conducted three complementary approaches.

(1) For each z-projected stack, we calculated the normalised histogram of local curvatures with a bin size of 0.05 μm^{-1} (Figure S8G) and averaged these histograms per condition (e.g., Figure 5B, red). The curvatures, expressed in per micrometer, range from 0.025 to 1 μm^{-1}, corresponding to curvature radii from 40 μm to 1 μm, respectively. 40 μm could be interpreted as mostly straight astral microtubules.

(2) We computed the 95th percentile curvature for each microtubule to capture faithfully the highest curvatures (Figure S6B1) and then took the median of the values over the microtubules of each z-projected stack. We finally compared the set of medians between two conditions (e.g., Figure 5D).

(3) We measured the tortuosity for each microtubule, defined as the curvilinear distance divided by the end-to-end distance (Figure S6C1). Straight microtubules have tortuosity values near one, while bent microtubules show higher values. Then, we calculated the medians of tortuosity for each z-projected stack and compared the set of medians between two conditions (e.g., Figure 5E).

M13- Fourier analysis of the positional micromovements

We investigated the micromovements of spindle position along the transverse axis over time, based on our previously published method[25]. From the time series of the spindle position along the transverse axis during anaphase obtained by tracking the poles (cf. M7), we computed the power spectral density (*PSD*) of the signal multiplied by the Hann window to safeguard against artefact due to the position difference between the beginning and end of the considered time interval[175]. It contrasted with [25], where we selected only embryos with low drift in their position over time, rather than windowing. The Hann windows appeared to be a sensible choice for fitting the *PSD* later since its discrete Fourier transform has only three non-zero coefficients[175, 176]. Therefore, once convolved to the real *PSD* of the spindle length, it minimally "blurs" it.

We then fitted this *PSD* with a second-order Lorentzian model, as in [25]. Along a mechanistic line, this model corresponds to a Kelvin-Voigt-with-inertia discrete model corresponding to a

Hookean spring (centring, K), a dashpot (damping, G), and an inertial element (I) in parallel. However, these quantities, when retrieved by fitting, depend on the amplitude of the stochastic noise that powers the fluctuations. We, therefore, utilised an alternative representation featuring (1) a diffusion coefficient D, inversely proportional to the damping G and dependent on the stochastic noise powering the fluctuations[25], (2) the centring-to-damping corner frequency f_c ($\propto K/G$) reflecting centring efficiency, and (3) the damping-to-inertia corner frequency f_0 ($\propto G/I$); the inertia I arising from load-dependent detachment of force generators as for anaphase rocking[57]. Such a model was transformed into the Fourier space and convolved on the fly with the transform of the Hann window to perform the fit[175]. We then performed the fit using augmented Lagrangians and refined it using the pattern search algorithm[177, 178] as implemented in [175]. To quantify the variability from biological origin of the spectrum over N embryos, we estimated the confidence interval at significance 0.05 using bootstrap with bias-corrected and accelerated percentile method[179, 180]. In particular, it involved performing 30 iterations of fitting a set of N embryos drawn with replacement from the available ones. We filtered out 4/30 draws in the case of non-treated paired with *zyg-8* overexpression as the fit resulted in a too-low likelihood.

M14- Statistics

The difference between two samples was assessed by the two-tailed Student's t-test with Welch–Satterthwaite correction for unequal variance. When Gaussian distribution cannot be assumed, we used the Mann–Whitney test (also known as the Wilcoxon rank-sum test). We used it for instance to compare microtubule highest curvatures (e.g., Figure 5D) or microtubule tortuosity (e.g., Figure 5E). For the sake of simplicity, we reported confidence levels using diamond (◊, $0.01 < p \leq 0.05$), stars (*, $0.001 < p \leq 0.01$; **, $1\text{x}10^{-4} < p \leq 0.001$; ***, $1\text{x}10^{-5} < p \leq 1\text{x}10^{-4}$) or ns (non-significant, $p > 0.05$). We abbreviated the standard deviation by SD. Last, we used the Kolmogorov–Smirnov test to reveal whether the two distributions differed significantly (distributions of contact durations or of local curvatures).

Acknowledgements

Some *Caenorhabditis elegans* strains were provided by the Caenorhabditis Genetics Center (CGC), which is funded by National Institutes of Health Office of Research Infrastructure Programs (P40 OD010440; University of Minnesota). Strains TH27 and TH30 were kindly offered by Prof Anthony A. Hyman. We thank Dr Grégoire Michaux for supplying the feeding clone library and for technical support. The CRISPR strains MCP347, MCP361 & MCP554 were generated by SeGiCel facility (CNRS UMS3453 - INSERM US7). We thank S. Dutertre and X. Pinson of the Microscopy Rennes Imaging Center (MRic, BIOSIT, Biogenouest) for their assistance. MRic is part of the national infrastructure France-BioImaging supported by the French National Research Agency (ANR-10-INBS-04). In particular, we acknowledge funding for the Zeiss Airyscan confocal microscope through EU FEDER (CARE Phase 2), the Zeiss Airyscan 2 confocal microscope via INCA, Rennes Métropole, CPER and Biosit, and the Nikon Nsparc confocal microscope through grants from INSERM (G. Michaux), ANR (GroBluRe, G. Michaux), and AIS Rennes Métropole (H. Boukhatmi). The spinning disc microscope was co-funded by the CNRS, Rennes Metropole (AIS 16C0400) and Region Bretagne (AniDyn-MT grant). L.C. was supported by a PhD fellowship from "La Ligue Nationale Contre le Cancer"

(2021-2024). H.B. was supported by the ANR grant MICENN, and by “La Ligue Régionale Contre le Cancer » (Ille-et-Vilaine & Deux-Sèvres committees, 2019 ; Côtes d’Armor & Ille-et-Vilaine committees, 2021), as well as the University of Rennes (Défis scientifiques, 2019). We thank the Pécréaux lab for their support, and the Gibeaux, Giet, Huet, Michaux, and Tramier labs for helpful discussions. We also thank L. Chesneau for assistance in designing the CRISPR strains, and A. Pacquelet, B. Lacroix and C. Heligon for their careful reading of the manuscript.

Author contributions

Conceptualisation: HB, JP; Experimental data: LC, EH, LS, SP, MC, TS, HB; Data curation: HB; Formal analysis: LC, EH, MC, JP, HB; Funding acquisition: JP, HB; Methodology: LC, JP, HB; Project administration: HB; Software: JP, HB; Supervision: JP, HB; Validation: LC, EH, JP, HB; Visualisation: LC, HB; Writing – original draft: HB; Writing – review and editing: LC, JP, HB.

Disclosure and competing interests statement

The authors declare that they have no conflict of interest.

REFERENCES

1. Matis, M. The Mechanical Role of Microtubules in Tissue Remodeling. *BioEssays* **42**, 1900244 (2020).
2. Rizzelli, F., Malabarba, M.G., Sigismund, S. & Mapelli, M. The crosstalk between microtubules, actin and membranes shapes cell division. *Open Biology* **10**, 190314 (2020).
3. Burute, M. & Kapitein, L.C. Cellular Logistics: Unraveling the Interplay Between Microtubule Organization and Intracellular Transport. *Annual Review of Cell and Developmental Biology* **35**, 29-54 (2019).
4. Garcin, C. & Straube, A. Microtubules in cell migration. *Essays in Biochemistry* **63**, 509-520 (2019).
5. McNally, F.J. Mechanisms of spindle positioning. *The Journal of cell biology* **200**, 131-140 (2013).
6. Forth, S. & Kapoor, T.M. The mechanics of microtubule networks in cell division. *J Cell Biol* **216**, 1525-1531 (2017).
7. Kotak, S. Mechanisms of Spindle Positioning: Lessons from Worms and Mammalian Cells. *Biomolecules* **9**, 80 (2019).
8. Thomas, G.E., Renjith, M.R. & Manna, T.K. Kinetochore–microtubule interactions in chromosome segregation: lessons from yeast and mammalian cells. *Biochemical Journal* **474**, 3559-3577 (2017).
9. Lechler, T. & Mapelli, M. Spindle positioning and its impact on vertebrate tissue architecture and cell fate. *Nature Reviews Molecular Cell Biology* **22**, 691-708 (2021).
10. di Pietro, F., Echard, A. & Morin, X. Regulation of mitotic spindle orientation: an integrated view. *EMBO reports* (2016).
11. van Leen, E.V., di Pietro, F. & Bellaïche, Y. Oriented cell divisions in epithelia: from force generation to force anisotropy by tension, shape and vertices. *Current Opinion in Cell Biology* **62**, 9-16 (2020).
12. Goodson, H.V. & Jonasson, E.M. Microtubules and microtubule-associated proteins. *Cold Spring Harbor perspectives in biology* **10**, a022608 (2018).
13. Akhmanova, A. & Kapitein, L.C. Mechanisms of microtubule organization in differentiated animal cells. *Nature Reviews Molecular Cell Biology* **23**, 541-558 (2022).
14. Gudimchuk, N.B. & McIntosh, J.R. Regulation of microtubule dynamics, mechanics and function through the growing tip. *Nature Reviews Molecular Cell Biology* **22**, 777-795 (2021).
15. Gittes, F., Mickey, B., Nettleton, J. & Howard, J. Flexural rigidity of microtubules and actin filaments measured from thermal fluctuations in shape. *The Journal of cell biology* **120**, 923-934 (1993).
16. Mickey, B. & Howard, J. Rigidity of microtubules is increased by stabilizing agents. *The Journal of cell biology* **130**, 909-917 (1995).
17. Felgner, H., Frank, R. & Schliwa, M. Flexural rigidity of microtubules measured with the use of optical tweezers. *Journal of Cell Science* **109**, 509-516 (1996).
18. Kurachi, M., Hoshi, M. & Tashiro, H. Buckling of a single microtubule by optical trapping forces: direct measurement of microtubule rigidity. *Cell motility and the cytoskeleton* **30**, 221-228 (1995).
19. Brangwynne, C.P. *et al.* Microtubules can bear enhanced compressive loads in living cells because of lateral reinforcement. *The Journal of cell biology* **173**, 733-741 (2006).

20. Zhang, Z., Nishimura, Y. & Kanchanawong, P. Extracting microtubule networks from superresolution single-molecule localization microscopy data. *Molecular biology of the cell* **28**, 333-345 (2017).
21. Hawkins, T., Mirigian, M., Yasar, M.S. & Ross, J.L. Mechanics of microtubules. *Journal of biomechanics* **43**, 23-30 (2010).
22. Balabanian, L., Berger, C.L. & Hendricks, A.G. Acetylated Microtubules Are Preferentially Bundled Leading to Enhanced Kinesin-1 Motility. *Biophysical journal* **113**, 1551-1560 (2017).
23. Daga, R.R., Yonetani, A. & Chang, F. Asymmetric Microtubule Pushing Forces in Nuclear Centering. *Current Biology* **16**, 1544-1550 (2006).
24. Tran, P., Marsh, L., Doye, V., Inoue, S. & Chang, F. A mechanism for nuclear positioning in fission yeast based on microtubule pushing. *The Journal of cell biology* **153**, 397-412 (2001).
25. Pécréaux, J. *et al.* The Mitotic Spindle in the One-Cell C. elegans Embryo Is Positioned with High Precision and Stability. *Biophysical journal* **111**, 1773-1784 (2016).
26. Meaders, J.L., de Matos, S.N. & Burgess, D.R. A Pushing Mechanism for Microtubule Aster Positioning in a Large Cell Type. *Cell Reports* **33**, 108213 (2020).
27. Garzon-Coral, C., Fantana, H.A. & Howard, J. A force-generating machinery maintains the spindle at the cell center during mitosis. *Science* **352**, 1124-1127 (2016).
28. Tolic-Nørrelykke, I.M., Sacconi, L., Thon, G. & Pavone, F.S. Positioning and elongation of the fission yeast spindle by microtubule-based pushing. *Current biology* **14**, 1181-1186 (2004).
29. Schneider, M.W.G. *et al.* A mitotic chromatin phase transition prevents perforation by microtubules. *Nature* (2022).
30. Maiato, H., Gomes, A.M., Sousa, F. & Barisic, M. Mechanisms of Chromosome Congression during Mitosis. *Biology* **6**, 13 (2017).
31. Arjona, M.I., Najafi, J. & Minc, N. Cytoplasm mechanics and cellular organization. *Current Opinion in Cell Biology* **85**, 102278 (2023).
32. Felgner, H. *et al.* Domains of neuronal microtubule-associated proteins and flexural rigidity of microtubules. *The Journal of cell biology* **138**, 1067-1075 (1997).
33. Nishida, K. *et al.* Effects of three microtubule-associated proteins (MAP2, MAP4, and Tau) on microtubules' physical properties and neurite morphology. *Scientific Reports* **13**, 8870 (2023).
34. Jean, D.C., Baas, P.W. & Black, M.M. A novel role for doublecortin and doublecortin-like kinase in regulating growth cone microtubules. *Human molecular genetics* **21**, 5511-5527 (2012).
35. Moores, C.A. *et al.* Mechanism of microtubule stabilization by doublecortin. *Molecular cell* **14**, 833-839 (2004).
36. Fourniol, F.J. *et al.* Template-free 13-protofilament microtubule–MAP assembly visualized at 8 Å resolution. *The Journal of Cell Biology* **191**, 463-470 (2010).
37. Pampaloni, F. *et al.* Thermal fluctuations of grafted microtubules provide evidence of a length-dependent persistence length. *Proceedings of the National Academy of Sciences* **103**, 10248-10253 (2006).
38. Sui, H. & Downing, K.H. Structural basis of interprotofilament interaction and lateral deformation of microtubules. *Structure* **18**, 1022-1031 (2010).

39. Hahn, I. *et al.* Tau, XMAP215/Msps and Eb1 co-operate interdependently to regulate microtubule polymerisation and bundle formation in axons. *PLOS Genetics* **17**, e1009647 (2021).
40. Kadavath, H. *et al.* Tau stabilizes microtubules by binding at the interface between tubulin heterodimers. *Proceedings of the National Academy of Sciences* **112**, 7501-7506 (2015).
41. Kellogg, E.H. *et al.* Near-atomic model of microtubule-tau interactions. *Science* **360**, 1242-1246 (2018).
42. Srayko, M., Kaya, A., Stamford, J. & Hyman, A.A. Identification and Characterization of Factors Required for Microtubule Growth and Nucleation in the Early C. elegans Embryo. *Developmental Cell* **9**, 223-236 (2005).
43. Dema, A. *et al.* Doublecortin reinforces microtubules to promote growth cone advance in soft environments. *Current Biology* (2024).
44. Bunker, J.M., Wilson, L., Jordan, M.A. & Feinstein, S.C. Modulation of microtubule dynamics by tau in living cells: implications for development and neurodegeneration. *Molecular biology of the cell* **15**, 2720-2728 (2004).
45. Shu, T. *et al.* Doublecortin-like kinase controls neurogenesis by regulating mitotic spindles and M phase progression. *Neuron* **49**, 25-39 (2006).
46. Vreugdenhil, E. *et al.* Doublecortin-like, a microtubule-associated protein expressed in radial glia, is crucial for neuronal precursor division and radial process stability. *European Journal of Neuroscience* **25**, 635-648 (2007).
47. Kaplan, A. & Reiner, O. Linking cytoplasmic dynein and transport of Rab8 vesicles to the midbody during cytokinesis by the doublecortin domain-containing 5 protein. *Journal of cell science* **124**, 3989-4000 (2011).
48. Gönczy, P. *et al.* zyg-8, a gene required for spindle positioning in C. elegans, encodes a doublecortin-related kinase that promotes microtubule assembly. *Developmental cell* **1**, 363 (2001).
49. Li, W., Crellin, H.A., Cheerambathur, D. & McNally, F.J. Redundant microtubule crosslinkers prevent meiotic spindle bending to ensure diploid offspring in C. elegans. *PLOS Genetics* **19**, e1011090 (2023).
50. Czajkowski, E.R., Zou, Y., Divekar, N.S. & Wignall, S.M. The doublecortin-family kinase ZYG-8DCLK1 regulates microtubule dynamics and motor-driven forces to promote the stability of C. elegans acentrosomal spindles. *PLOS Genetics* **20**, e1011373 (2024).
51. Couillard-Despres, S. *et al.* Mitotic impairment by doublecortin is diminished by doublecortin mutations found in patients. *Neurogenetics* **5**, 83-93 (2004).
52. Rossi, G. *et al.* A new function of microtubule-associated protein tau: involvement in chromosome stability. *Cell Cycle* **7**, 1788-1794 (2008).
53. Bougé, A.-L. & Parmentier, M.-L. Tau excess impairs mitosis and kinesin-5 function, leading to aneuploidy and cell death. *Disease Models & Mechanisms* **9**, 307-319 (2016).
54. Liu, J.S. *et al.* Molecular basis for specific regulation of neuronal kinesin-3 motors by doublecortin family proteins. *Molecular cell* **47**, 707-721 (2012).
55. Rose, L. & Gönczy, P. Polarity establishment, asymmetric division and segregation of fate determinants in early C. elegans embryos. *WormBook: the online review of C. elegans biology*, 1-43 (2013).
56. Oegema, K. & Hyman, T. Cell division. *WormBook: The Online Review of C. elegans Biology* (2006).

57. Pécréaux, J. *et al.* Spindle Oscillations during Asymmetric Cell Division Require a Threshold Number of Active Cortical Force Generators. *Current Biology* **16**, 2111-2122 (2006).
58. Kozlowski, C., Srayko, M. & Nedelec, F. Cortical microtubule contacts position the spindle in C. elegans embryos. *Cell* **129**, 499-510 (2007).
59. Wu, H.-Y. *et al.* Laser ablation and fluid flows reveal the mechanism behind spindle and centrosome positioning. *Nature Physics* (2023).
60. Grill, S.W., Kruse, K. & Jülicher, F. Theory of Mitotic Spindle Oscillations. *Physical Review Letters* **94**, 108104 (2005).
61. Valfort, A.-C., Launay, C., Sémon, M. & Delattre, M. Evolution of mitotic spindle behavior during the first asymmetric embryonic division of nematodes. *PLoS Biology* **16**, e2005099 (2018).
62. Riche, S. *et al.* Evolutionary comparisons reveal a positional switch for spindle pole oscillations in Caenorhabditis embryos. *The Journal of cell biology* **201**, 653-662 (2013).
63. Bouvrais, H. *et al.* Microtubule Feedback and LET-99-Dependent Control of Pulling Forces Ensure Robust Spindle Position. *Biophysical journal* **115**, 2189-2205 (2018).
64. Howard, J. & Garzon-Coral, C. Physical Limits on the Precision of Mitotic Spindle Positioning by Microtubule Pushing forces. *BioEssays* **39**, 1700122 (2017).
65. Nguyen-Ngoc, T., Afshar, K. & Gonczy, P. Coupling of cortical dynein and G[alpha] proteins mediates spindle positioning in Caenorhabditis elegans. *Nat Cell Biol* **9**, 1294-1302 (2007).
66. Grill, S.W. & Hyman, A.A. Spindle positioning by cortical pulling forces. *Developmental Cell* **8**, 461-465 (2005).
67. Kimura, K. & Kimura, A. Intracellular organelles mediate cytoplasmic pulling force for centrosome centration in the Caenorhabditis elegans early embryo. *Proceedings of the National Academy of Sciences* **108**, 137-142 (2011).
68. Howard, J. Elastic and damping forces generated by confined arrays of dynamic microtubules. *Physical biology* **3**, 54 (2006).
69. Grill, S.W., Howard, J., Schaffer, E., Stelzer, E.H.K. & Hyman, A.A. The distribution of active force generators controls mitotic spindle position. *Science* **301**, 518 (2003).
70. Farhadifar, R. *et al.* Stoichiometric interactions explain spindle dynamics and scaling across 100 million years of nematode evolution. *Elife* **9**, e55877 (2020).
71. Bouvrais, H. *et al.* The coordination of spindle-positioning forces during the asymmetric division of the Caenorhabditis elegans zygote. *EMBO reports* **22**, e50770 (2021).
72. Bellanger, J.-M. *et al.* ZYG-9, TAC-1 and ZYG-8 together ensure correct microtubule function throughout the cell cycle of C. elegans embryos. *Journal of Cell Science* **120**, 2963-2973 (2007).
73. Agulto, R.L. *et al.* Autoregulatory control of microtubule binding in doublecortin-like kinase 1. *Elife* **10**, e60126 (2021).
74. Wood, W.B. *et al.* Parental effects and phenotypic characterization of mutations that affect early development in Caenorhabditis elegans. *Developmental Biology* **74**, 446-469 (1980).
75. Srayko, M., Quintin, S., Schwager, A. & Hyman, A.A. Caenorhabditis elegans TAC-1 and ZYG-9 form a complex that is essential for long astral and spindle microtubules. *Current biology: CB* **13**, 1506 (2003).

76. Brouhard, G.J. *et al.* XMAP215 Is a Processive Microtubule Polymerase. *Cell* **132**, 79-88 (2008).
77. Piehl, M., Tulu, U.S., Wadsworth, P. & Cassimeris, L. Centrosome maturation: measurement of microtubule nucleation throughout the cell cycle by using GFP-tagged EB1. *Proceedings of the National Academy of Sciences* **101**, 1584-1588 (2004).
78. Decker, M. *et al.* Limiting Amounts of Centrosome Material Set Centrosome Size in C. elegans Embryos. *Current Biology* **21**, 1259-1267 (2011).
79. Baumgart, J. *et al.* Soluble tubulin is significantly enriched at mitotic centrosomes. *Journal of Cell Biology* **218**, 3977-3985 (2019).
80. Woodruff, J.B. *et al.* Regulated assembly of a supramolecular centrosome scaffold in vitro. *Science* **348**, 808-812 (2015).
81. Horesh, D. *et al.* Doublecortin, a stabilizer of microtubules. *Human molecular genetics* **8**, 1599-1610 (1999).
82. Moores, C.A. *et al.* Distinct roles of doublecortin modulating the microtubule cytoskeleton. *The EMBO Journal* **25**, 4448-4457 (2006).
83. Manka, S.W. & Moores, C.A. Pseudo-repeats in doublecortin make distinct mechanistic contributions to microtubule regulation. *EMBO reports* **21**, e51534 (2020).
84. Espiritu, E.B., Krueger, L.E., Ye, A. & Rose, L.S. CLASPs function redundantly to regulate astral microtubules in the C. elegans embryo. *Developmental biology* **368**, 242-254 (2012).
85. Al-Bassam, J. *et al.* CLASP promotes microtubule rescue by recruiting tubulin dimers to the microtubule. *Developmental Cell* **19**, 245-258 (2010).
86. Walczak, C.E., Gayek, S. & Ohi, R. Microtubule-Depolymerizing Kinesins. *Annual Review of Cell and Developmental Biology* **29**, 417-441 (2013).
87. Cheeseman, I.M., MacLeod, I., Yates, J.R., Oegema, K. & Desai, A. The CENP-F-like Proteins HCP-1 and HCP-2 Target CLASP to Kinetochores to Mediate Chromosome Segregation. *Current Biology* **15**, 771-777 (2005).
88. Edwards, F., Maton, G., Gareil, N., Canman, J.C. & Dumont, J. BUB-1 promotes amphitelic chromosome biorientation via multiple activities at the kinetochore. *Elife* **7**, e40690 (2018).
89. Grill, S.W., Gönczy, P., Stelzer, E.H.K. & Hyman, A.A. Polarity controls forces governing asymmetric spindle positioning in the Caenorhabditis elegans embryo. *Nature* **409**, 630-633 (2001).
90. Grill, S.W., GoÈnczy, P., Stelzer, E.H.K. & Hyman, A.A. Polarity controls forces governing asymmetric spindle positioning in theCaenorhabditis elegansembryo. (2001).
91. Bellanger, J.-M. *et al.* The doublecortin-related gene zyg-8 is a microtubule organizer in Caenorhabditis elegans neurons. *Journal of Cell Science* **125**, 5417-5427 (2012).
92. Nedelec, F. & Foethke, D. Collective Langevin dynamics of flexible cytoskeletal fibers. *New Journal of Physics* **9**, 427 (2007).
93. Tsitkov, S. *et al.* The rate of microtubule breaking increases exponentially with curvature. *Scientific Reports* **12**, 20899 (2022).
94. Odde, D.J., Ma, L., Briggs, A.H., DeMarco, A. & Kirschner, M.W. Microtubule bending and breaking in living fibroblast cells. *Journal of Cell Science* **112**, 3283-3288 (1999).
95. Bicek, A.D. *et al.* Anterograde Microtubule Transport Drives Microtubule Bending in LLC-PK1 Epithelial Cells. *Molecular biology of the cell* **20**, 2943-2953 (2009).

96. Kikumoto, M., Kurachi, M., Tosa, V. & Tashiro, H. Flexural rigidity of individual microtubules measured by a buckling force with optical traps. *Biophysical journal* **90**, 1687-1696 (2006).
97. Kurz, J.C. & Williams Jr, R.C. Microtubule-associated proteins and the flexibility of microtubules. *Biochemistry* **34**, 13374-13380 (1995).
98. Venier, P., Maggs, A.C., Carlier, M.-F. & Pantaloni, D. Analysis of microtubule rigidity using hydrodynamic flow and thermal fluctuations. *Journal of biological chemistry* **269**, 13353-13360 (1994).
99. Blob, A. *et al.* Global alignment and local curvature of microtubules in mouse fibroblasts are robust against perturbations of vimentin and actin. *Soft matter* (2025).
100. McDermott, J.B., Aamodt, S. & Aamodt, E. ptl-1, a Caenorhabditis elegans gene whose products are homologous to the τ microtubule-associated proteins. *Biochemistry* **35**, 9415-9423 (1996).
101. Goedert, M. *et al.* PTL-1, a microtubule-associated protein with tau-like repeats from the nematode Caenorhabditis elegans. *Journal of cell science* **109**, 2661-2672 (1996).
102. Tintori, Sophia C., Osborne Nishimura, E., Golden, P., Lieb, Jason D. & Goldstein, B. A Transcriptional Lineage of the Early C. elegans Embryo. *Developmental Cell* **38**, 430-444 (2016).
103. Glotzer, M. The 3Ms of central spindle assembly: microtubules, motors and MAPs. *Nature Reviews Molecular Cell Biology* **10**, 9-20 (2009).
104. Maurer, S.P., Fourniol, F.J., Bohner, G., Moores, C.A. & Surrey, T. EBs recognize a nucleotide-dependent structural cap at growing microtubule ends. *Cell* **149**, 371-382 (2012).
105. Manka, Szymon W. & Moores, Carolyn A. Microtubule structure by cryo-EM: snapshots of dynamic instability. *Essays In Biochemistry* (2018).
106. Bechstedt, S. & Brouhard, G.J. Doublecortin recognizes the 13-protofilament microtubule cooperatively and tracks microtubule ends. *Developmental Cell* **23**, 181-192 (2012).
107. Ettinger, A., van Haren, J., Ribeiro, Susana A. & Wittmann, T. Doublecortin Is Excluded from Growing Microtubule Ends and Recognizes the GDP-Microtubule Lattice. *Current Biology* **26**, 1549-1555 (2016).
108. Tsuchiya, K. & Goshima, G. Microtubule-associated proteins promote microtubule generation in the absence of γ-tubulin in human colon cancer cells. *Journal of Cell Biology* **220** (2021).
109. Rogers, G., Rusan, N., Peifer, M. & Rogers, S. A Multicomponent Assembly Pathway Contributes to the Formation of Acentrosomal Microtubule Arrays in Interphase Drosophila Cells. *Molecular biology of the cell* **19**, 3163-3178 (2008).
110. Lin, P.T., Gleeson, J.G., Corbo, J.C., Flanagan, L. & Walsh, C.A. DCAMKL1 Encodes a Protein Kinase with Homology to Doublecortin that Regulates Microtubule Polymerization. *The Journal of Neuroscience* **20**, 9152-9161 (2000).
111. Tint, I., Jean, D., Baas, P.W. & Black, M.M. Doublecortin associates with microtubules preferentially in regions of the axon displaying actin-rich protrusive structures. *Journal of Neuroscience* **29**, 10995-11010 (2009).
112. Kim, M.H. *et al.* The DCX-domain tandems of doublecortin and doublecortin-like kinase. *Nature Structural & Molecular Biology* **10**, 324-333 (2003).
113. Bielas, S.L. *et al.* Spinophilin Facilitates Dephosphorylation of Doublecortin by PP1 to Mediate Microtubule Bundling at the Axonal Wrist. *Cell* **129**, 579-591 (2007).

114. Redemann, S. *et al.* C. elegans chromosomes connect to centrosomes by anchoring into the spindle network. *Nature Communications* **8**, 15288 (2017).
115. Portran, D., Schaedel, L., Xu, Z., Théry, M. & Nachury, Maxence V. Tubulin acetylation protects long-lived microtubules against mechanical ageing. *Nature Cell Biology* **19**, 391 (2017).
116. Wall, K.P. *et al.* C-Terminal Tail Polyglycylation and Polyglutamylation Alter Microtubule Mechanical Properties. *Biophysical journal* **119**, 2219-2230 (2020).
117. Xu, Z. *et al.* Microtubules acquire resistance from mechanical breakage through intralumenal acetylation. *Science* **356**, 328-332 (2017).
118. Nishi, K. *et al.* Nonequilibrium bending fluctuations reveal microtubule mechanics in-vivo and their regulation by glutamylation. *bioRxiv*, 2023.2010.2026.564252 (2023).
119. Robison, P. *et al.* Detyrosinated microtubules buckle and bear load in contracting cardiomyocytes. *Science* **352**, aaf0659 (2016).
120. Sébastien, M., Paquette, A.L., Prowse, E.N.P., Hendricks, A.G. & Brouhard, G.J. Doublecortin restricts neuronal branching by regulating tubulin polyglutamylation. *Nature Communications* **16**, 1749 (2025).
121. Chawla, D.G. *et al.* Caenorhabditis elegans glutamylating enzymes function redundantly in male mating. *Biology Open* **5**, 1290-1298 (2016).
122. Schaedel, L. *et al.* Microtubules self-repair in response to mechanical stress. *Nature Materials* **14**, 1156-1163 (2015).
123. Aher, A. *et al.* CLASP Mediates Microtubule Repair by Restricting Lattice Damage and Regulating Tubulin Incorporation. *Current Biology* **30**, 2175-2183.e2176 (2020).
124. Théry, M. & Blanchoin, L. Microtubule self-repair. *Current Opinion in Cell Biology* **68**, 144-154 (2021).
125. Chrétien, D., Metoz, F., Verde, F., Karsenti, E. & Wade, R.H. Lattice defects in microtubules: protofilament numbers vary within individual microtubules. *The Journal of cell biology* **117**, 1031-1040 (1992).
126. Schaedel, L. *et al.* Lattice defects induce microtubule self-renewal. *Nature Physics* (2019).
127. Chaaban, S. *et al.* The Structure and Dynamics of C. elegans Tubulin Reveals the Mechanistic Basis of Microtubule Growth. *Developmental Cell* (2018).
128. Wu, J.C. & Rose, L.S. PAR-3 and PAR-1 inhibit LET-99 localization to generate a cortical band important for spindle positioning in Caenorhabditis elegans embryos. *Molecular biology of the cell* **18**, 4470-4482 (2007).
129. Redemann, S. *et al.* Membrane invaginations reveal cortical sites that pull on mitotic spindles in one-cell C. elegans embryos. *PloS one* **5**, e12301 (2010).
130. Fielmich, L.-E. *et al.* Optogenetic dissection of mitotic spindle positioning in vivo. *Elife* **7**, e38198 (2018).
131. Dogterom, M., Kerssemakers, J.W.J., Romet-Lemonne, G. & Janson, M.E. Force generation by dynamic microtubules. *Current Opinion in Cell Biology* **17**, 67-74 (2005).
132. Bergstralh, D.T., Dawney, N.S. & St Johnston, D. Spindle orientation: a question of complex positioning. *Development* **144**, 1137-1145 (2017).
133. Jingchen, L., Longcan, C. & Hongyuan, J. Cell shape and intercellular adhesion regulate mitotic spindle orientation. *Molecular biology of the cell* **30**, 2458-2468 (2019).
134. Mao, Y. *et al.* Planar polarization of the atypical myosin Dachs orients cell divisions in Drosophila. *Genes Dev* **25**, 131-136 (2011).

135. Strauss, B., Adams, R.J. & Papalopulu, N. A default mechanism of spindle orientation based on cell shape is sufficient to generate cell fate diversity in polarised Xenopus blastomeres. *Development* **133**, 3883-3893 (2006).
136. Tsou, M.F.B., Hayashi, A., DeBella, L.R., McGrath, G. & Rose, L.S. LET-99 determines spindle position and is asymmetrically enriched in response to PAR polarity cues in C. elegans embryos. *Development* **129**, 4469-4481 (2002).
137. Singh, D., Schmidt, N., Müller, F., Bange, T. & Bird, A.W. Destabilization of Long Astral Microtubules via Cdk1-Dependent Removal of GTSE1 from Their Plus Ends Facilitates Prometaphase Spindle Orientation. *Current Biology* **31**, 766-781.e768 (2021).
138. Saleh, J. *et al.* Length limitation of astral microtubules orients cell divisions in murine intestinal crypts. *Developmental Cell* **58**, 1519-1533.e1516 (2023).
139. Izumi, Y., Ohta, N., Hisata, K., Raabe, T. & Matsuzaki, F. Drosophila Pins-binding protein Mud regulates spindle-polarity coupling and centrosome organization. *Nature cell biology* **8**, 586-593 (2006).
140. Siller, K.H., Cabernard, C. & Doe, C.Q. The NuMA-related Mud protein binds Pins and regulates spindle orientation in Drosophila neuroblasts. *Nature Cell Biology* **8**, 594-600 (2006).
141. Williams, S.E., Beronja, S., Pasolli, H.A. & Fuchs, E. Asymmetric cell divisions promote Notch-dependent epidermal differentiation. *Nature* **470**, 353-358 (2011).
142. Fischer, E. *et al.* Defective planar cell polarity in polycystic kidney disease. *Nature Genetics* **38**, 21-23 (2006).
143. Fleming, E.S., Temchin, M., Wu, Q., Maggio-Price, L. & Tirnauer, J.S. Spindle misorientation in tumors from APC mice. *Molecular Carcinogenesis* **48**, 592-598 (2009).
144. Pease, J.C. & Tirnauer, J.S. Mitotic spindle misorientation in cancer – out of alignment and into the fire. *Journal of Cell Science* **124**, 1007-1016 (2011).
145. Quesada-Hernández, E. *et al.* Stereotypical Cell Division Orientation Controls Neural Rod Midline Formation in Zebrafish. *Current Biology* **20**, 1966-1972 (2010).
146. Baena-López, L.A., Baonza, A. & García-Bellido, A. The Orientation of Cell Divisions Determines the Shape of Drosophila Organs. *Current Biology* **15**, 1640-1644 (2005).
147. Quyn, A.J. *et al.* Spindle Orientation Bias in Gut Epithelial Stem Cell Compartments Is Lost in Precancerous Tissue. *Cell Stem Cell* **6**, 175-181 (2010).
148. Gao, L. *et al.* Afadin orients cell division to position the tubule lumen in developing renal tubules. *Development* **144**, 3511-3520 (2017).
149. Fededa, J.P. *et al.* MicroRNA-34/449 controls mitotic spindle orientation during mammalian cortex development. *The EMBO Journal* **35**, 2386-2398 (2016).
150. Gao, T. *et al.* DCLK1 is up-regulated and associated with metastasis and prognosis in colorectal cancer. *J Cancer Res Clin Oncol* **142**, 2131-2140 (2016).
151. Ge, Y. *et al.* Alternative splice variants of DCLK1 mark cancer stem cells, promote self-renewal and drug-resistance, and can be targeted to inhibit tumorigenesis in kidney cancer. *Int J Cancer* **143**, 1162-1175 (2018).
152. Ito, H. *et al.* Dominant expression of DCLK1 in human pancreatic cancer stem cells accelerates tumor invasion and metastasis. *PLoS One* **11**, e0146564 (2016).
153. Liu, H. *et al.* DCLK1 plays a metastatic-promoting role in human breast cancer cells. *BioMed Research International* **2019** (2019).
154. Rossi, G. *et al.* Tau mutations serve as a novel risk factor for cancer. *Cancer research* **78**, 3731-3739 (2018).

155. Gargini, R., Segura-Collar, B. & Sánchez-Gómez, P. Novel Functions of the Neurodegenerative-Related Gene Tau in Cancer. *Frontiers in Aging Neuroscience* **11** (2019).
156. Papin, S. & Paganetti, P. Emerging Evidences for an Implication of the Neurodegeneration-Associated Protein TAU in Cancer. *Brain Sciences* **10**, 862 (2020).
157. Brenner, S. The genetics of Caenorhabditis elegans. *Genetics* **77**, 71-94 (1974).
158. Kamath, R.S. & Ahringer, J. Genome-wide RNAi screening in Caenorhabditis elegans. *Methods* **30**, 313-321 (2003).
159. Duerr, J.S. Antibody staining in C. elegans using "freeze-cracking". *J Vis Exp* (2013).
160. Li, S. *et al.* Metadata management for high content screening in OMERO. *Methods* **96**, 27-32 (2016).
161. Costes, S.V. *et al.* Automatic and quantitative measurement of protein-protein colocalization in live cells. *Biophysical journal* **86**, 3993-4003 (2004).
162. Bolte, S. & Cordelières, F.P. A guided tour into subcellular colocalization analysis in light microscopy. *Journal of Microscopy* **224**, 213-232 (2006).
163. Schindelin, J. *et al.* Fiji: an open-source platform for biological-image analysis. *Nature methods* **9**, 676-682 (2012).
164. Pécréaux, J., Zimmer, C. & Olivo-Marin, J.-C. in Image Processing, 2006 IEEE International Conference on 1949-1952 (IEEE, 2006).
165. Kalman, R.E. A new approach to linear filtering and prediction problems. *Journal of basic Engineering* **82**, 35-45 (1960).
166. de Chaumont, F. *et al.* Icy: an open bioimage informatics platform for extended reproducible research. *Nature methods* **9**, 690 (2012).
167. Soler, N. *et al.* Kinesin-12 KLP-18 contributes to the kinetochore-microtubule poleward flux during the metaphase of C. elegans one-cell embryo. *bioRxiv*, 2022.2011.2007.515476 (2025).
168. Kolin, D. (2003).
169. Jaqaman, K. *et al.* Robust single-particle tracking in live-cell time-lapse sequences. *Nat Methods* **5**, 695-702 (2008).
170. Sugioka, K. *et al.* Tumor suppressor APC is an attenuator of spindle-pulling forces during C. elegans asymmetric cell division. *Proceedings of the National Academy of Sciences*, 201712052 (2018).
171. Forster, B., Van De Ville, D., Berent, J., Sage, D. & Unser, M. in Biomedical Imaging: Nano to Macro, 2004. IEEE International Symposium on 660-663 (IEEE, 2004).
172. Sandberg, K. & Brega, M. Segmentation of thin structures in electron micrographs using orientation fields. *Journal of Structural Biology* **157**, 403-415 (2007).
173. Bicek, A.D., Tüzel, E., Kroll, D.M. & Odde, D.J. Analysis of Microtubule Curvature, in *Methods in Cell Biology*, Vol. 83 237-268 (Academic Press, 2007).
174. Kroon, D.-J. (Mathworks, 2011).
175. Mercat, B., Vol. PhD (Univesité de rennes 1, 2016).
176. harris, f. On the Use of Windows for Harmonic Analysis With the Discrete Fourier Transform. *Proceedings of the IEEE* **66**, 51-83 (1978).
177. Pierre, D.A. & Lowe, M.J. Mathematical programming via augmented lagrangians: An introduction with computer programs. *(No Title)* (1975).
178. Audet, C. & Dennis Jr, J.E. Analysis of generalized pattern searches. *SIAM Journal on optimization* **13**, 889-903 (2002).

179. DiCiccio, T.J. & Efron, B. Bootstrap confidence intervals. *Statistical science* **11**, 189-228 (1996).
180. Efron, B. & Tibshirani, R.J. *An introduction to the bootstrap*. (Chapman and Hall/CRC, 1994).

Main figures & table

From the article: “Microtubule stiffening by ZYG-8 contributes to spindle orientation during *C. elegans* zygote division”; Cueff L. *et al.*, 2025.

Conditions	Frequency interval	D (m^2/s)	f_c (Hz)	f_0 (Hz)
RNAi control (N = 15)	0.03 -> 0.3 Hz	1.7×10^{-13} [$0.7 - 15.0 \times 10^{-13}$]	0.86 [0.03 - 6.68]	3.1×10^{-3} [$0.4 - 51.4 \times 10^{-3}$]
zyg-8(RNAi) (N = 20)		1.3×10^{-13} [$0.7 - 166 \times 10^{-13}$]	0.18 [0.13 - 5.78]	4.2×10^{-3} [$0.1 - 7.4 \times 10^{-3}$]
ptl-1(RNAi) (N = 13)		1.0×10^{-13} [$0.8 - 4.9 \times 10^{-13}$]	0.34 [0.09 - 5.46]	5.9×10^{-3} [$0.1 - 83.3 \times 10^{-3}$]
Untreated at the restrictive temperature (N = 11)	0 -> 0.5 Hz	7.3×10^{-14} [$5.8 - 9.0 \times 10^{-14}$]	0.19 [0.15 - 0.22]	1.3×10^{-2} [$1.1 - 1.5 \times 10^{-2}$]
zyg-8(or484ts) at the restrictive temperature (N = 12)		11.3×10^{-14} [$6.2 - 687.9 \times 10^{-14}$]	0.9×10^{-3} [$0.89\ 0.95 \times 10^{-3}$]	1.3×10^{-2} [$0.01 - 2.4 \times 10^{-2}$]

Table 1: Mechanical parameters measured during anaphase, including the diffusion coefficient (D) and two corner frequencies (f_c and f_0). They were obtained by fitting the experimental power spectra of spindle positional micromovements along the transverse axis within the specified frequency interval using a second-order model (Method M13). The confidence intervals were estimated by the bootstrap resampling method with significance level 0.05.

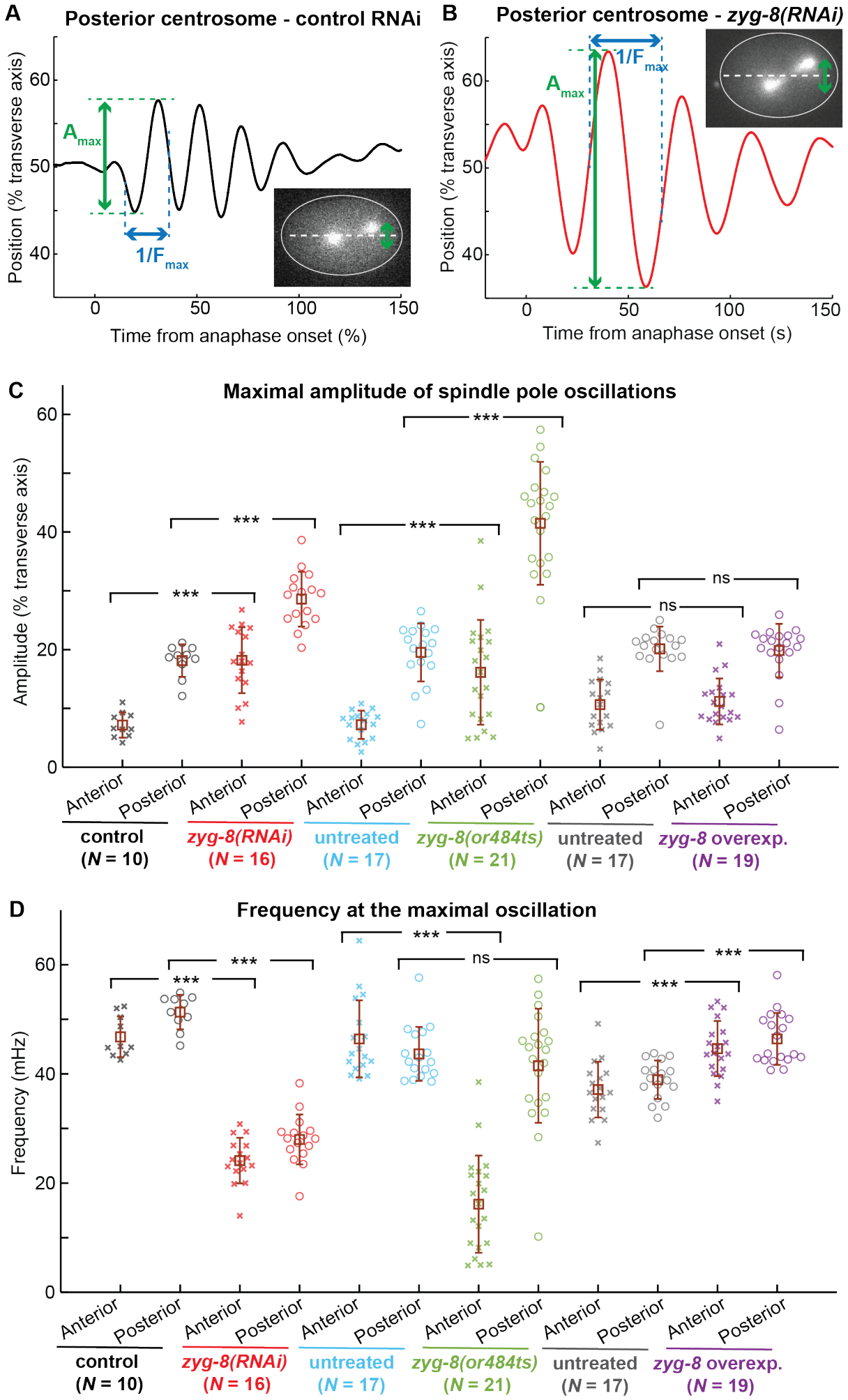
A
Posterior centrosome - control RNAi
Position (% transverse axis)
Time from anaphase onset (%)
A max
1/F max
B
Posterior centrosome - zyg-8(RNAi)
Position (% transverse axis)
Time from anaphase onset (s)
C
Maximal amplitude of spindle pole oscillations
Amplitude (% transverse axis)
***
ns
Anterior
Posterior
control (N = 10)
zyg-8(RNAi) (N = 16)
untreated (N = 17)
zyg-8(or484ts) (N = 21)
untreated (N = 17)
zyg-8 overexp. (N = 19)
D
Frequency at the maximal oscillation
Frequency (mHz)

Figure 1: ZYG-8 limits spindle-pole oscillation amplitudes and increases their frequencies during anaphase.

(**A-B**) Exemplar posterior-centrosome positions along the transverse axis for (A) a control RNAi embryo and (B) a *zyg-8(RNAi)* treated embryo. Maximal amplitudes are highlighted in green, while their frequencies are annotated in blue. We applied a moving-average filter over a window size of 5 s to smooth the centrosome positions. Exemplar images used for centrosome analysis with a GFP::TBB-2 fluorescent labelling. (**C**) Maximal oscillation amplitudes and (**D**) their frequencies for the (cross) anterior and (circle) posterior centrosomes during anaphase. We tracked the centrosomes and analysed their positions in: (red) N = 16 *zyg-8(RNAi)* treated embryos and (black) N = 10 control embryos; (light green) N = 21 *zyg-8(or484ts)* mutants and (light blue) N = 17 untreated embryos, both at the restrictive temperature; (purple) N = 19 *zyg-8* overexpressing embryos and (grey) N = 17 untreated embryos (Method M7). The brown squares and error bars correspond to the means and SD (Method M14).

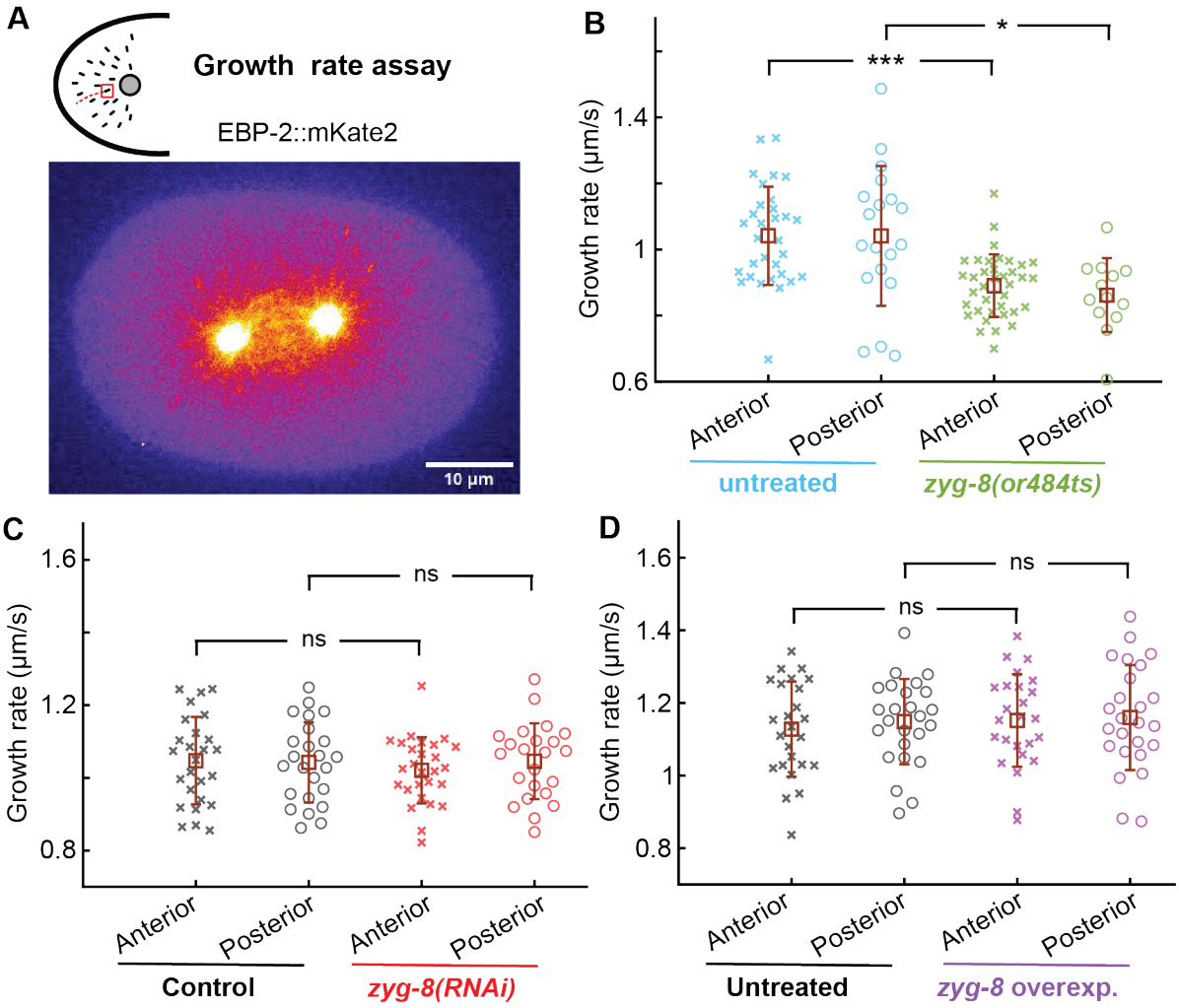

Figure 2: ZYG-8 modestly promotes microtubule growth.
(**A**) Microtubule growth rate assay by tracking comets in embryos whose microtubule plus-ends were fluorescently labelled with EBP-2::mKate2 (Method M8). Example of a RNAi control embryo processed with Kalman denoising, a preprocessing step performed prior to quantification. (**B-D**) Growth rates of astral microtubules measured at (cross) anterior and (circle) posterior centrosomes: (B) (light green) *N* = 37 comets from microtubules emanating from the anterior centrosome and *N* = 13 comets from posterior centrosome in 10 *zyg-8(or484ts)* mutants, and (light blue) *N* = 31 comets from anterior-centrosome and *N* = 19 posterior-centrosome comets in 13 untreated embryos both at the restrictive temperature; (C) (red) *N* = 27 comets from anterior centrosome and *N* = 23 comets from posterior centrosome in 10 *zyg-8(RNAi)* treated embryos, and (black) *N* = 26 comets from anterior centrosome and *N* = 24 comets from posterior centrosome in 8 control embryos; (D) (purple) *N* = 25 comets from anterior centrosome and *N* = 25 comets from posterior centrosome in 10 *zyg-8* overexpressing embryos and (black) *N* = 25 comets from anterior centrosome and *N* = 25 comets from posterior centrosome in 10 untreated embryos. The brown squares and error bars correspond to the means and SD (Method M14).

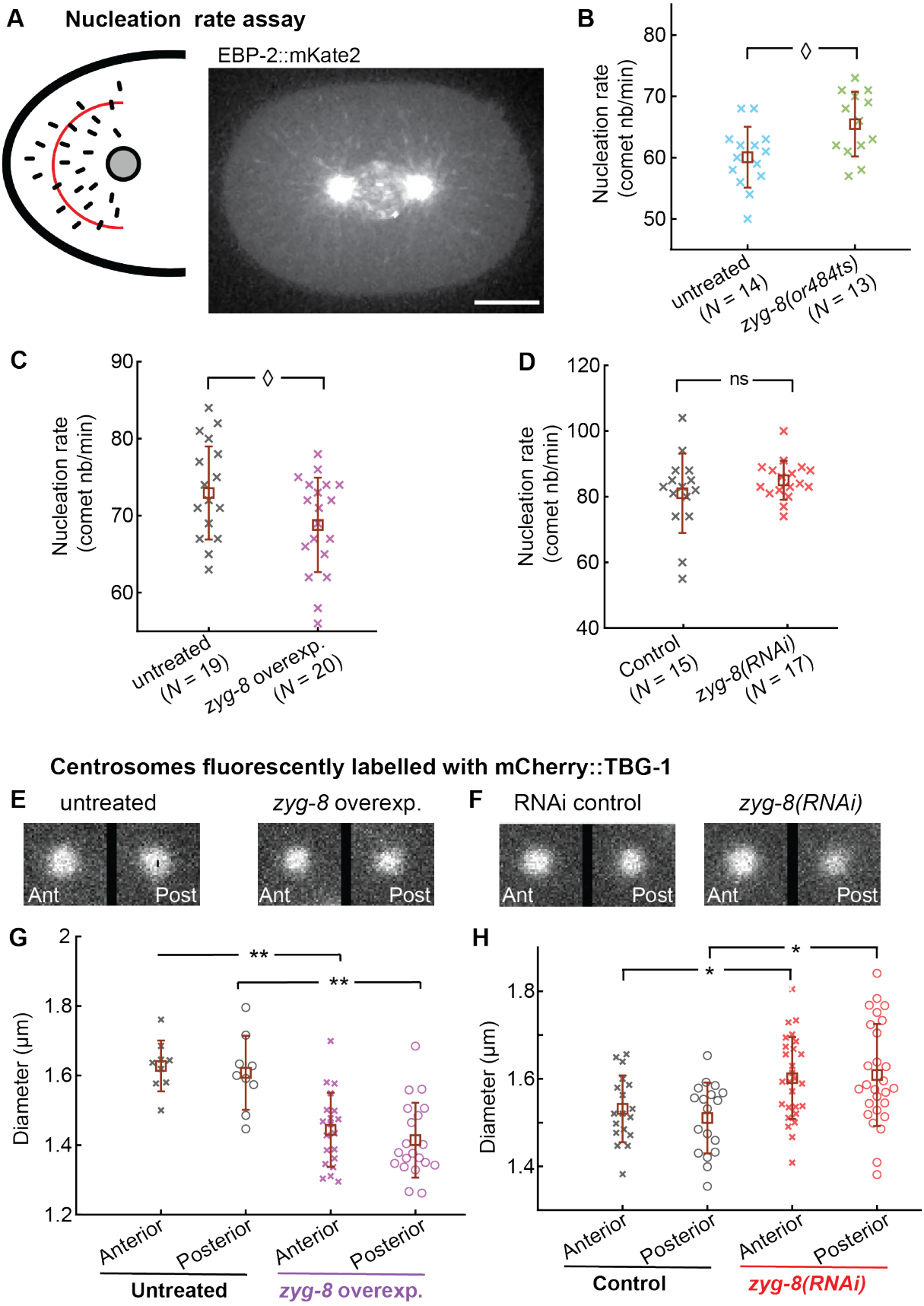

Figure 3: ZYG-8 limits microtubule nucleation, albeit modestly.

(**A**) Microtubule nucleation rate assay by counting comets crossing a half-circle region of interest positioned 9 µm from the centrosome in embryos whose microtubule plus-ends were fluorescently

labelled using EBP-2::mKate2 (Method M8). Example of a RNAi control embryo processed with Candle denoising, a preprocessing step performed prior to comet counting. Scale bars represent 10 μm. **(B-D)** Nucleation rates of the astral microtubules with *N* indicating the number of analysed centrosomes per condition: (A) (light green) N_e = 8 *zyg-8(or484ts)* mutants and (light blue) N_e = 9 untreated embryos, both at the restricted temperature; (B) (purple) N_e = 10 *zyg-8* overexpressing embryos and (black) N_e = 10 untreated embryos; (C) (red) N_e = 10 *zyg-8(RNAi)* treated embryos and (black) N_e = 8 control embryos. (**E-F**) Regions centred on the centrosomes (40 x 40 pixels; 6.4 x 6.4 μm) from exemplar microscopy images showing centrosomes fluorescently labelled with mCherry::TBG-1: (E) representative images of untreated and *zyg-8* overexpressing embryos; (F) representative images of RNAi control and *zyg-8(RNAi)* treated embryos. **(G-H**) Diameters during metaphase of (cross) anterior and (circle) posterior centrosomes (Method M9): (G) (purple) N_e = 21 *zyg-8* overexpressing embryos and (black) N_e = 9 untreated embryos; (H) (red) N_e = 27 *zyg-8(RNAi)* treated embryos and (black) N_e = 18 control embryos. The brown squares and error bars correspond to the means and SD (Method M14).

Dynamics of astral microtubules at the cell cortex of *C. elegans* zygote

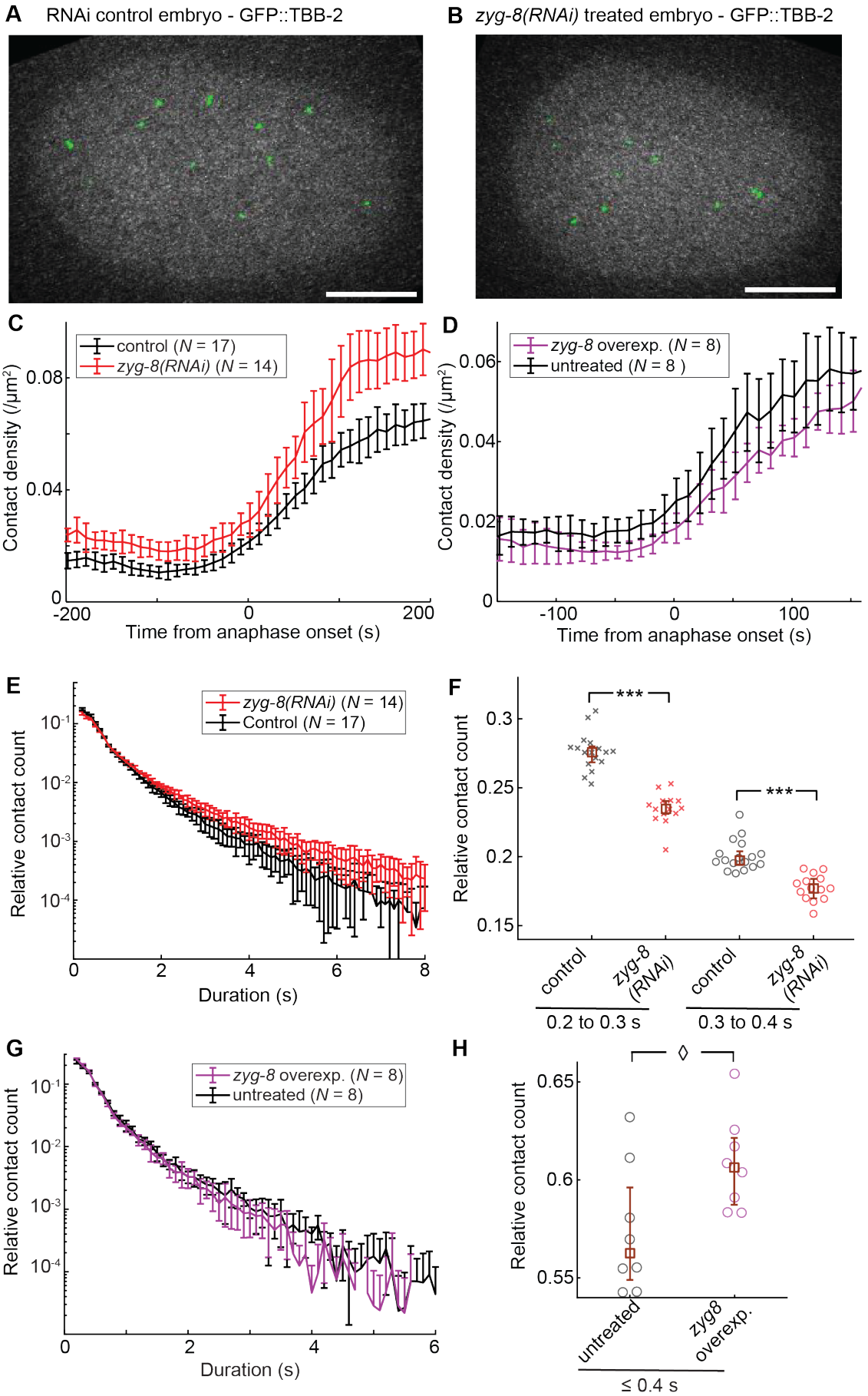

Figure 4: Perturbations in microtubule dynamics at the cell cortex upon targeting *zyg-8* does not support a role for ZYG-8 in stabilising microtubules.

(**A-B**) Embryos whose microtubules are labelled by GFP::TBB-2 and imaged at the cortical plane (Method M4): examples of (A) a RNAi control embryo (Movie S1), and (B) a *zyg-8(RNAi)* treated embryo (Movie S2) at anaphase onset. Green spots highlight the detected contacts (Method M10). Scale bars represent 10 μm. (**C-D**) Embryo-averaged density of astral microtubule contacts at the cortex plane along mitosis. We tracked and analysed the cortical contacts of microtubules labelled: (C) by GFP::TBB-2 in (red) N =14 *zyg-8(RNAi)* treated embryos and (black) N = 17 control ones; (D) by mCherry::tubulin in (purple) N = 8 *zyg-8* overexpressing embryos and (black) N = 8 untreated ones. (**E**) Embryo-averaged distributions of cortical lifetimes of astral microtubules during metaphase (Kolmogorov–Smirnov test: $p = 6\text{x}10^{-4}$, Methods M10 and M14). Embryos are the same as in panel C. (**F**) Relative contact counts for the two shortest duration bins (0.2 to 0.3 s & 0.3 to 0.4 s) from the distributions presented in panel E, highlighting differences in brief contact durations. (**G**) Embryo-averaged distributions of cortical lifetimes of astral microtubules during metaphase (Kolmogorov–Smirnov test: $p = 0.18$, Methods M10 and M14). Embryos are the same as in panel D. (**H**) Relative counts of contacts with durations below 0.4 s, highlighting variations in short-lived durations. Data were derived from the distributions in panel G. Representative movies of each of the four present conditions are provided as Movies S1-S4. Microtubule contacts were tracked using u-track (Method M10). The brown squares and error bars correspond to the medians and the quartiles (Method M14).

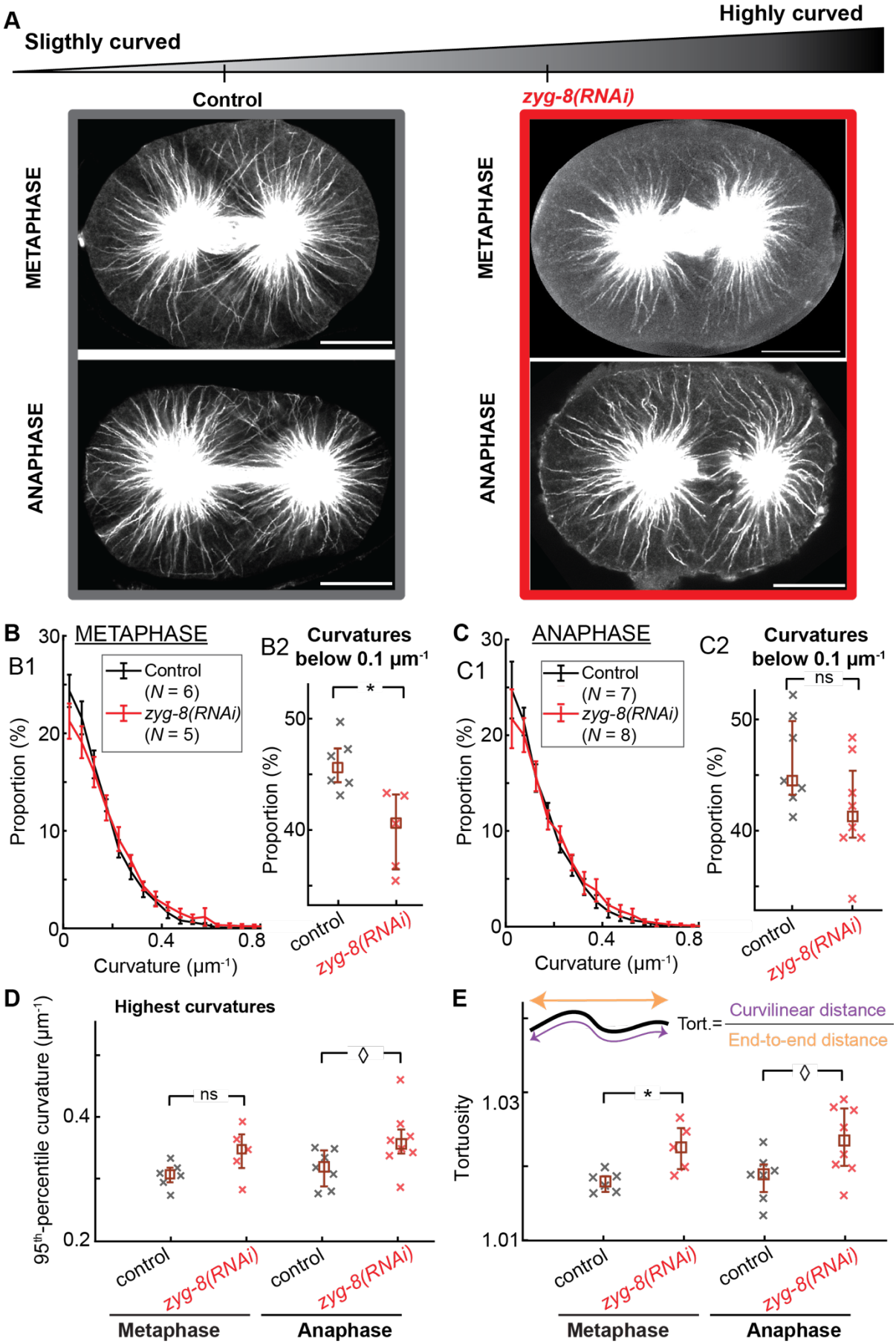
A
Sligthly curved
Highly curved
Control
zyg-8(RNAi)
METAPHASE
ANAPHASE
METAPHASE
ANAPHASE
B
B1
METAPHASE
Control (N = 6)
zyg-8(RNAi) (N = 5)
Proportion (%)
Curvature (µm-1)
B2
Curvatures below 0.1 µm-1
*
Proportion (%)
control
zyg-8(RNAi)
C
C1
ANAPHASE
Control (N = 7)
zyg-8(RNAi) (N = 8)
Proportion (%)
Curvature (µm-1)
C2
Curvatures below 0.1 µm-1
ns
Proportion (%)
control
zyg-8(RNAi)
D
Highest curvatures
95th-percentile curvature (µm-1)
ns
◊
control
zyg-8(RNAi)
control
zyg-8(RNAi)
Metaphase
Anaphase
E
Tort.= Curvilinear distance / End-to-end distance
Tortuosity
*
◊
control
zyg-8(RNAi)
control
zyg-8(RNAi)
Metaphase
Anaphase

Figure 5: Astral microtubule tortuosity and curvatures slightly increase upon *zyg-8(RNAi)*.
(**A**) The deconvolved confocal images of fixed embryos with α-tubulin immunostaining reveal microtubule shapes during (top row) metaphase or (bottom row) anaphase in (left) control embryos, and (right) *zyg-8(RNAi)* treated embryos (Methods M3 and M4). The scale bars represent 10 μm. (**B-C**) Averaged distributions of astral microtubule local curvatures of (red) *zyg-8(RNAi)* treated embryos and (black) control embryos: (B1) during metaphase with (red) N = 5 z-projected stacks and (black) N = 6 z-projected stacks (Kolmogorov–Smirnov test: p = 0.36, Method M14); and (C1) during anaphase with (red) N = 8 z-projected stacks and (black) N = 7 z-projected stacks (Kolmogorov–Smirnov test: p = 0.36, Method M14). (B2, C2) Focus on the proportions of low local curvatures ($\leq$ 0.01 μm^{-1}) for the same embryos as in panels B1 & C1. (**D**) Medians per z-projected stacks of the highest curvatures (measured as 95th percentile curvature) during metaphase (data are the same as in panel B) and during anaphase (data are the same as in panel C). (**E**) Medians per z-projected stacks of microtubule tortuosity during metaphase using the same embryos as in panels B &D, and during anaphase using the same embryos as in panels C & D. Embryos were fixed and immuno-stained for α-tubulin; microtubules were segmented; and local curvature and tortuosity were computed (Methods M3, M4, M12). The brown squares and error bars correspond to the medians and the quartiles (Method M14).

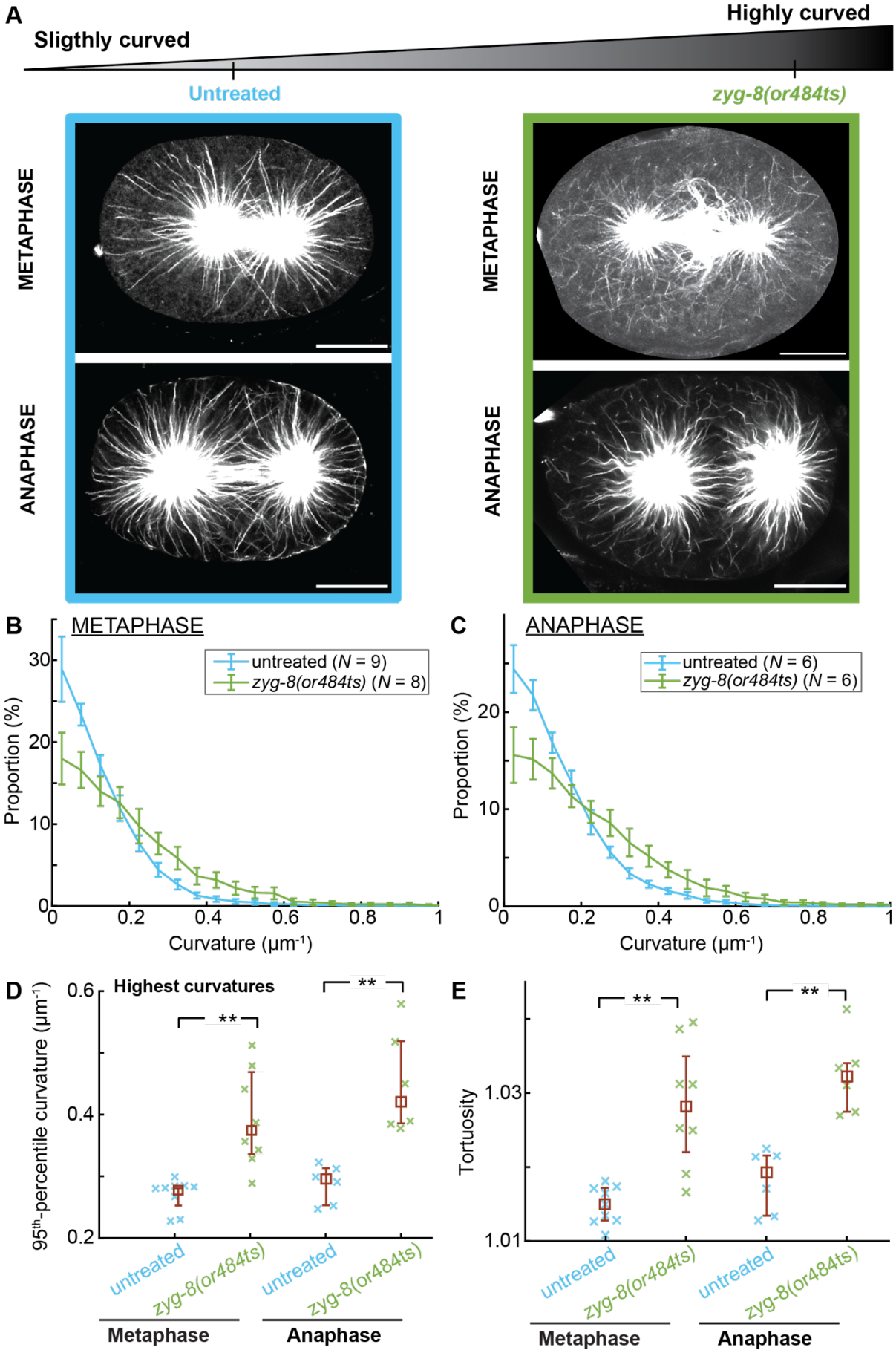
A
Sligthly curved
Highly curved
Untreated
zyg-8(or484ts)
METAPHASE
ANAPHASE
METAPHASE
ANAPHASE
B
METAPHASE
untreated (N = 9)
zyg-8(or484ts) (N = 8)
Proportion (%)
Curvature (μm-1)
C
ANAPHASE
untreated (N = 6)
zyg-8(or484ts) (N = 6)
Proportion (%)
Curvature (μm-1)
D
Highest curvatures
95th-percentile curvature (μm-1)
**
**
untreated
zyg-8(or484ts)
untreated
zyg-8(or484ts)
Metaphase
Anaphase
E
Tortuosity
**
**
untreated
zyg-8(or484ts)
untreated
zyg-8(or484ts)
Metaphase
Anaphase

Figure 6: Astral microtubules appear more curved and tortuous in *zyg-8(or484ts)* mutants.
(**A**) The deconvolved confocal images of fixed embryos with α-tubulin immunostaining reveal microtubule shapes during (top row) metaphase or (bottom row) anaphase in (left) untreated embryos, and (right) *zyg-8(or484ts)* mutant embryos, both at the restrictive temperature (Methods M3 and M4). The scale bars represent 10 μm. **(B-C)** Averaged distributions of astral microtubule local curvatures of (light green) *zyg-8(or484ts)* mutants and (light blue) untreated embryos, both at the restrictive temperature: (B) during metaphase with (light green) N = 8 z-projected stacks and (light blue) N = 9 z-projected stacks (Kolmogorov–Smirnov test: p = 0.03, Method M14); and (C) during anaphase with (light green) N = 6 z-projected stacks and (light blue) N = 6 z-projected stacks (Kolmogorov–Smirnov test: p = 0.014, Method M14). (**D**) Medians per z-projected stacks of the highest curvatures (measured as 95th percentile curvature) during metaphase (data are the same as in panel B) and during anaphase (data are the same as in panel C). (**E**) Medians per z-projected stacks of microtubule tortuosity during metaphase using the same embryos as in panel B &D, and during anaphase using the same embryos as in panels C & D. Embryos were fixed and immuno-stained for α-tubulin; microtubules were segmented; and local curvature and tortuosity were computed (Methods M3, M4, M12). The brown squares and error bars correspond to the medians and the quartiles (Method M14).

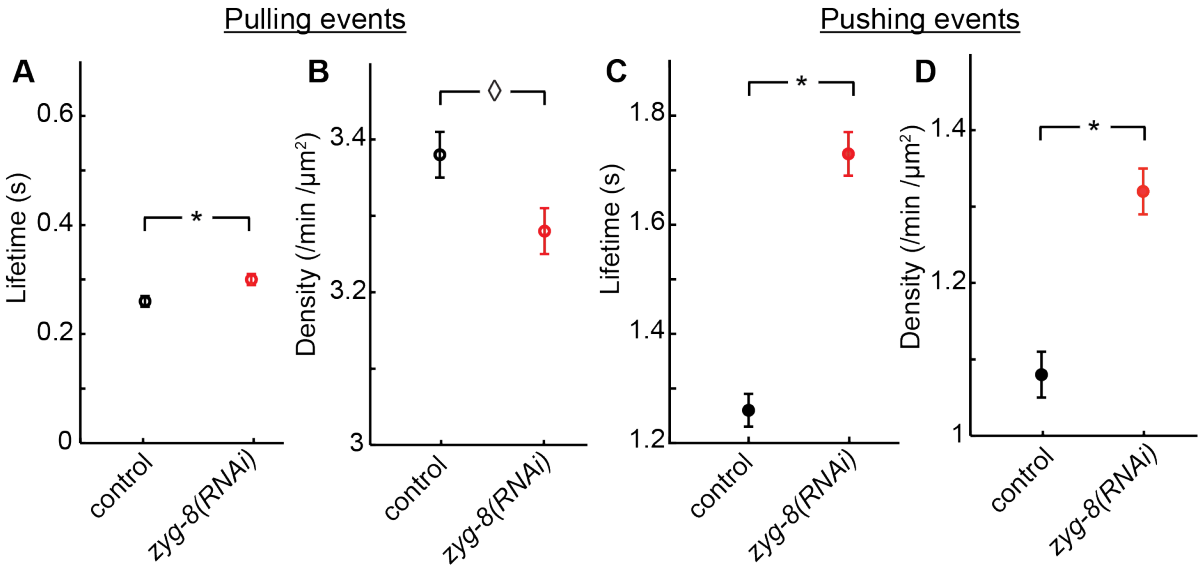

Figure 7: Depleting ZYG-8 weakens highly the cortical pushing events.
(**A**) Lifetimes and (**B**) densities of the cortical pulling events, and (**C**) lifetimes and (**D**) densities of the cortical pushing events. We tracked and analysed the microtubule contacts at the cell cortex using a GFP::TBB-2 fluorescent labelling in (red) *N* = 14 *zyg-8(RNAi)* treated embryos and (black) *N* = 17 control embryos (same embryos as for Figure 4C, E & F) (Methods M10 & M14).

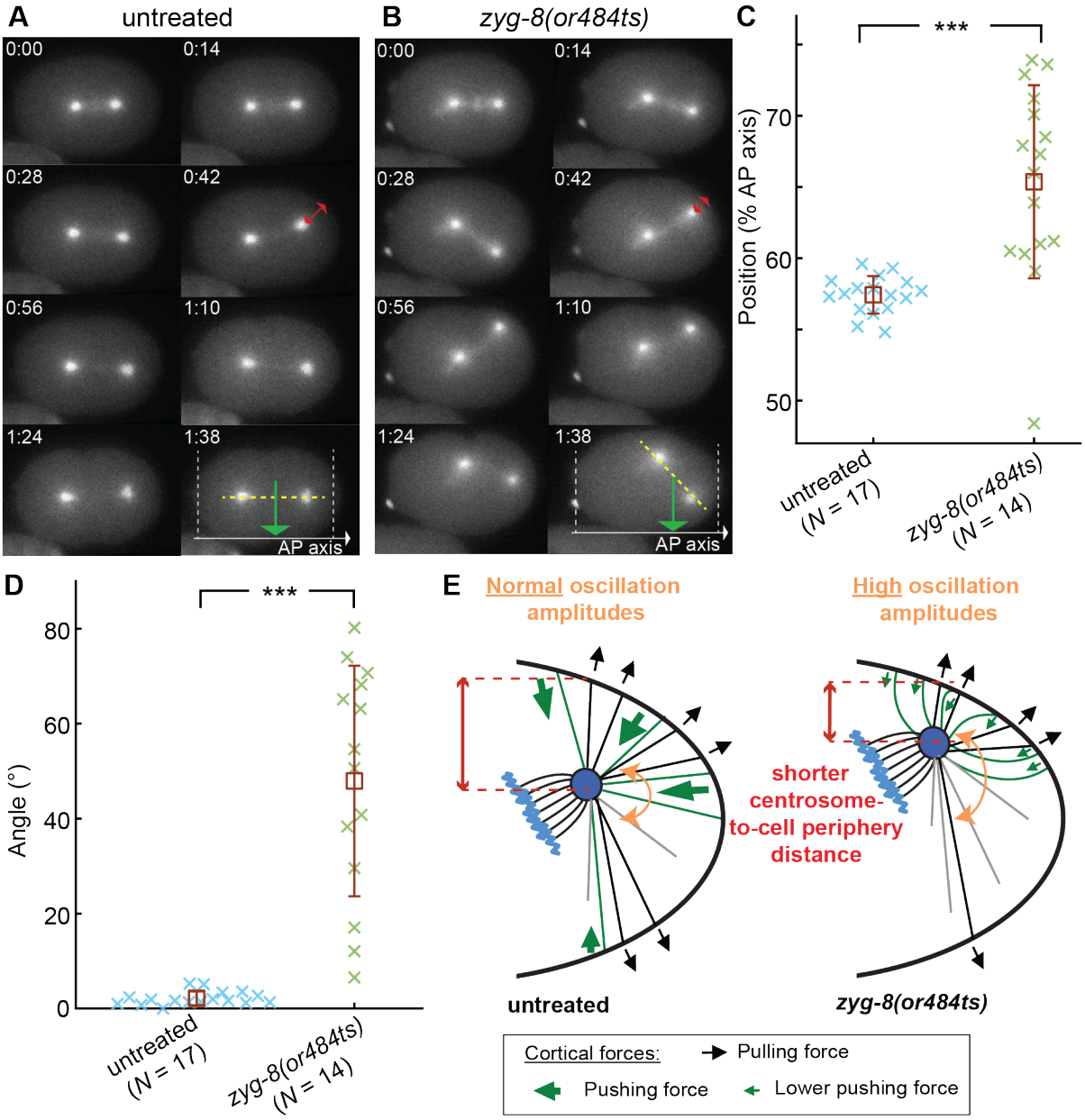

Figure 8: In *zyg-8(or484ts)* mutants, overly soft microtubules result in a misoriented and mispositioned spindle at the anaphase end.

(**A-B**) Time-lapse series of (A) an exemplar untreated embryo and (B) an exemplar *zyg-8(or484ts)* mutant along anaphase, both at the restrictive temperature and with EBP-2::mKate2 labelling. The green arrows indicate the spindle's final positions along the anteroposterior (AP) axis and the dotted yellow lines indicate the final orientations. The red double-headed arrows underline the minimal centrosome-to-cortex distances. The scale bars represent 10 µm. (**C-D**) Spindle final (C) positions along the AP axis and (D) angles for (light green) N = 14 *zyg-8(or484ts)* mutants and (light blue) N = 17 untreated embryos, both at the restrictive temperature. We tracked and analysed the centrosomes of embryos with EBP-2::mKate2 labelling (Method M7). The brown squares and error bars correspond to the means and SD (Method M14). (**E**) Schematics illustrating how a large reduction in microtubule flexural rigidity could lead to spindle positioning and orientation defects.